Electronic Theses and Dissertations

12-2018

The migration and developmental remodeling of intrinsic interneurons in visual thalamus and the role of retinal signaling.

Naomi E. Charalambakis
University of Louisville

THE MIGRATION AND DEVELOPMENTAL REMODELING OF
INTRINSIC INTERNEURONS IN VISUAL THALAMUS
AND THE ROLE OF RETINAL SIGNALING

By

Naomi E. Charalambakis
B.S., University of Kentucky, 2013
M.S., University of Louisville, 2017

A Dissertation
Submitted to the Faculty of the
School of Medicine of the University of Louisville
in Partial Fulfillment of the Requirements
for the Degree of

Doctor of Philosophy
In Anatomical Sciences and Neurobiology

Department of Anatomical Sciences and Neurobiology
University of Louisville
Louisville, Kentucky

December 2018

THE MIGRATION AND DEVELOPMENTAL REMODELING OF INTRINSIC
INTERNEURONS IN VISUAL THALAMUS AND
THE ROLE OF RETINAL SIGNALING

By

Naomi E. Charalambakis
B.S., University of Kentucky, 2013
M.S., University of Louisville, 2017

A Dissertation Approved on:

October 16th, 2018

By the following members of the Dissertation Committee:

_____
William Guido, Ph.D.

_____
Martha Bickford, Ph.D.

_____
Robin Krimm, Ph.D.

_____
Aaron McGee, Ph.D.

_____
Michael Fox, Ph.D.

ii

DEDICATION

This dissertation is dedicated to my parents,

John and Fedra Charalambakis

ACKNOWLEDGEMENTS

ABSTRACT

THE MIGRATION AND DEVELOPMENTAL REMODELING OF INTRINSIC
INTERNEURONS IN VISUAL THALAMUS AND THE ROLE OF RETINAL
SIGNALING

Naomi E. Charalambakis

October FÎ ẼG̃ẽFì

The dorsal lateral geniculate nucleus (dLGN) of the mouse is a model

system to study the development of thalamic circuitry. While most studies focus

on relay neurons of dLGN, little is known about the factors regulating the

development of the other principal cell type, intrinsic interneurons. To date, the

targeting and migratory path of dLGN interneurons as well as their morphological

development remains unclear. Here we examined whether the migration,

structure, and function of interneurons relies on retinal signaling. We took a loss-of-

function approach and crossed GAD67-GFP mice, which express green

fluorescent protein (GFP) in dLGN interneurons, with *math5* nulls (math5$^{-/-}$),

mutants that lack retinofugal projections. Tracing studies with BDA show that

interneurons migrate from the third ventricle, and arrive in dLGN at early postnatal

ages. By P4, neurons complete the first phase of a multi-staged developmental

process, as interneuron number and distribution reaches an

v

adult-like state. *In-vitro* recordings and 3-D reconstructions of biocytin-filled interneurons at different ages showed that remodeling begins during the second week, and includes a period of exuberant branching, where arbors grow in number, complexity, and field size. Such growth is followed by pruning and stabilization, as interneurons adopt their adult-like bipolar architecture and form functional connections with relay cells. However, the absence of retinal signaling disrupts these processes. Fewer interneurons occupy dLGN, and cells fail to disperse. Estimates of interneuron number in thalamic nuclei along the migratory path in math5$^{-/-}$ mice suggest that the absence of retinal input causes misrouting of dLGN interneurons into the ventrobasal complex (VB). In fact, studies in Fibroblast growth factor 15 null (Fgf15$^{-/-}$) mice, a neurotrophic factor responsible for GABAergic differentiation, show Fgf15 regulates interneuron targeting to dLGN. Arbor remodeling is also disrupted in the absence of retinal signaling, as interneurons maintained a sparse architecture at all ages. DHPG experiments in math5$^{-/-}$ mice, the metabotropic glutamate receptor 1,5 (mGluR$_{1,5}$) agonist that targets F2 terminals on interneuron processes, revealed interneurons exhibited fewer/and or weaker synapses with relay neurons in dLGN. Taken together, these data suggest that retinal signaling is needed to support the targeting, arbor elaboration, and synaptic connectivity of dLGN interneurons.

TABLE OF CONTENTS

LIST OF FIGURES

INTRODUCTION

In the past decade, the mouse has surfaced as the model system of choice to examine the establishment and functional processes of visual thalamic circuits. One reason is because the mouse retinogeniculate pathway is highly conserved. Despite low acuity, the mouse exhibits parallel visual pathways that are well-separated, similar to higher mammals such as the cat and macaque (Reese, 1988). Secondly, the recent surge in new genetic tools such as transgenic mouse lines has provided unmatched access to specific cell types and circuits. For the first time, we are able to isolate and manipulate individual cells within the visual pathway to understand their development, structure, and function. Finally, the mouse affords us the ability to study vision in combination with behavioral function. Now with molecular tools and genetically-labeled mouse lines, studies can conceivably link particular behaviors and functions with the circuits and cells actively involved. Taken together, the mouse model has transformed the field of neuroscience, and will continue to advance our understanding of the visual thalamus.

In the mouse, the axons of retinal ganglion cells (RGCs) form the optic nerve/tract to exit the eye and project to the dorsal lateral geniculate nucleus (dLGN). These projections are highly organized to deliver an accurate

representation of the contralateral visual hemifield (Grubb and Thompson, 2003; Pfeiffenberger et al., 2006). Although mice do not have distinct laminae separating contralateral and ipsilateral eye projections as seen in carnivores and primates, retinal afferents in rodent are still organized into separate eye-specific domains (Reese, 1988). Another example of such conserved circuitry exhibited in the mouse is cell-type specificity and regional preferences in dLGN. Similar to all higher-order species, mice exhibit 2 primary cells: excitatory thalamocortical relay cells and inhibitory interneurons. Relay neurons are responsible for directly transferring visual signals from the retina to visual cortex (Martin, 1986), whereas interneurons remain intrinsic to dLGN and function as the neural stop-signs of the nucleus, ensuring retinogeniculate transmission remains balanced and linear by operating through feedforward connections (Williams et al., 1996; Sherman, 2004). Currently, we understand more about the development of relay neurons, whereas many more unanswered questions remain about dLGN interneurons. However, for both cell types, recent research has revealed numerous examples of the mouse's conserved visual circuitry, and has demonstrated why the mouse serves as a tractable experimental platform to understand the underlying mechanisms of vision.

Relay cells of the dLGN are characterized by their type I/Class A morphology, bearing a thick axon and multiple, complex dendrites emanating from its large, round soma. Additionally, analysis of their dendritic architecture reveal relay neurons are classified into three classes based on morphology—X-, Y-, and W-cells—similar to what's been found in the cat (Friedlander et al., 1981;

Stanford et al., 1981; Krahe et al., 2011). In fact, each class occupies specific regions within dLGN (Krahe et al., 2011). For example, W-cells exhibit a hemispheric structure, and reside along the dorsolateral, "shell" region of the nucleus (Bickford et al., 2015), the homologue of the C-laminae in cat and where most W-cells are found (Stanford et al., 1981; Sur and Sherman, 1982). Y-cells possess a concentric dendritic architecture, and occupy the central core region of dLGN that is binocularly innervated. Finally, X-cells have a biconical dendritic tree, and primarily reside in the ventral sector of dLGN. Such region specificity is a reflection of the projection patterns of difference RGC types. For example, direction-selective ganglion cells (DSGCs) largely project to the dorsolateral shell onto W-cells, and OFF-alpha transient ganglion cells connect with Y-cells in the core (Martin, 1986; Dhande et al., 2015).

Developmentally, relay neurons experience two growth spurts (Parnavelas et al., 1977; El-Danaf et al., 2015). The first takes place during the first postnatal week when dendritic branching and complexity increases. In fact, by the end of week 1, neurons have adopted their adult-like morphology and class specification. The second growth spurt occurs during the second and third postnatal week when the size of the dendritic field and the area of dLGN increases, with little change in branch number or complexity. There is also strong evidence suggesting that such growth is, in part, regulated by retinal innervation. One report studied relay cell development in a mouse that is devoid of retinal innervation, and discovered that their dendritic growth and maturation is disrupted. Although neurons maintain cell-class specificity, they also experience

an exuberant branching period, followed by branch elimination and a decline in dendritic field size (El-Danaf et al., 2015).

Our understanding about the other primary cell type, intrinsic interneurons, is an emerging story. Exhibiting a Type II/Class B morphology with spindle-shaped somata, dLGN interneurons form connections only with other dLGN neurons, and function to modulate excitatory signals from the retina by providing feedforward inhibition. Interneurons accomplish this by refining the center-surround receptive field properties of relay cells, sharpening the timing of excitatory responses, and shaping the spatial and temporal features of the visual scene (Sherman, 2004; Blitz and Regehr, 2005; Hirsch et al., 2015). Moreover, interneurons are equipped with unique structural features that allow them to operate as local, independent processors. Similar to other higher mammals, in addition to a typical axonal output (F1 terminals), embedded within interneuron dendritic trees are distal processes with grape-like appendages, the presumed site of F2 terminals and location of dendro-dendritic synapses. Oftentimes, F2 terminals participate in unique, triadic synaptic arrangements that involve a relay cell dendrite, F2 terminal, and retinal axon in contact with one another (Sherman, 2004; Bickford et al., 2010). Such inhibitory activity is electrically isolated from the soma, thus affording interneurons with the ability to integrate synaptic inputs locally (via dendrites) and/or globally (via axon) (Sherman, 2004; Govindaiah and Cox, 2006). This feedforward inhibition becomes apparent around the time of eye-opening (~P14), and is comprised of a $GABA_A$ and $GABA_B$ component. Such activity corresponds to the synaptic development of the mouse dLGN, as its

ultrastructure reaches adult-like patterns by P14 (Bickford et al., 2010). Furthermore, the synaptic organization of the mouse is highly conserved when compared to the make-up of other species such as rat, cat, and monkey (Wilson and Hendrickson, 1981; Gabbott et al., 1986; Montero, 1991).

There is evidence to suggest that there are two classes of interneurons, similar to relay cell class specification. In rat, interneurons have been classified based on NADPH Diaphorase immunoreactivity. Those that stained positive only for GABA are called B1 neurons, while cells that were both diaphorase and GABA positive are called B2 neurons (Gabbott and Bacon, 1994). Similarly, a study in cat demonstrates that dLGN interneurons can be classified based on brain nitric oxide synthase (BNOS). BNOS-stained interneurons were consistently found in the C-laminae (the homologue to the mouse dorsolateral tier), and possess larger somas compared to BNOS-negative interneurons. Additionally, ultrastructure analyses revealed that BNOS-positive interneurons participate in dendrodendritic synapses in extraglomerular neuropil, whereas their counterparts function within synaptic glomeruli (Hamos et al., 1985; Bickford et al., 1999). A recent study in mouse also suggests that dLGN interneurons are comprised of two classes. Interneurons are classified based on soma diameter, with smaller ones having a higher density of I_H channels and higher rates of firing compared to larger ones (Leist et al., 2016). While the issue of interneuron classification remains open to debate, information thus far provides support for the use of the mouse as a model system to study visual thalamic development.

As research continues to evolve about dLGN interneurons, it is worth emphasizing that compared to relay neurons, far less is known about their development, or the factors that influence their maturation. Such investigation has been hampered by the lack of available tools. In the past, researchers had difficulty visualizing interneurons, especially given the fact that in rodents, these cells comprise only 5-10% of neurons in dLGN (Arcelli et al., 1997; Evangelio et al., 2018). However, the mouse model has moved to the forefront of neuroscience research, and the advent of mouse transgenics affords us the ability to accomplish what we could not before. The discovery of the GAD67-GFP strain, a transgenic mouse line that expresses GFP in dLGN interneurons, allows us to visualize and target these cells for anatomical and electrophysiological examination. Because this expression is seen as early as embryonic age 15 (E15) (Tamamaki et al., 2003) it also permits for tracking progenitors as they differentiate into interneurons and migrate to target structures (Golding et al., 2014). Loss-of-function mouse models further provide the ability to isolate the cells and circuitry of different inhibitory pathways, and learn about their development and underlying mechanism (Seabrook et al., 2013; Golding et al., 2014; Jager et al., 2016). Thus, to address the remaining unknowns about dLGN interneurons, we took advantage of development of sophisticated genetic tools, and used the GAD67-GFP mouse to study the migratory path, distribution, morphological development, and synaptic connectivity of dLGN interneurons. Utilizing genetic knockout mice with the math5 null (math5$^{-/-}$) and Fgf15 null (Fgf15$^{-/-}$) mice allowed us to assess how retinal signaling influences these

developmental processes, and its underlying mechanism, respectively. Taken together, these studies will shed light on the establishment and integration of intrinsic interneurons into thalamus, and the factors that influence its timing and patterning.

CHAPTER I

RETINAL SIGNALING REGULATES THE TARGETING AND MIGRATION OF

INTRINSIC INTERNEURONS TO THE DORSAL LATERAL GENICULATE

NUCLEUS

Introduction

Much of our understanding about the development, form, and function of

thalamic circuits is derived from work done in the dorsal lateral geniculate

nucleus (dLGN) of the mouse (Jaubert-Miazza et al., 2005; Huberman et al.,

2008; Krahe et al., 2011; Hong et al., 2014). The dLGN serves as a relay of

visual signals between the retina and visual cortex, and is comprised of two

primary cell types, excitatory thalamocortical relay cells and intrinsic inhibitory

interneurons. While both types are innervated by the retina, only relay neurons

have axons that exit dLGN and project to visual cortex. Interneurons and their

processes are intrinsic to dLGN and form feedforward inhibitory connections with

relay cells (Guillery and Sherman 2002; Seabrook et al., 2013; Hirsch et al.,

2015). This inhibitory circuit serves to limit the spatial and temporal spread of

retinally-evoked excitatory activity in dLGN. Such activity results in the

sharpening of receptive field properties of relay neurons, and improving the

contrast-gain of retinogeniculate signal transmission (Norton and Godwin 1992; Sherman, 2004; Blitz and Regehr, 2005; Hirsch et al., 2015).

To date, relay neurons have been the principal focus for understanding thalamic operations, but the generation of a transgenic GFP mouse line that labels thalamic interneurons has led to a number of important discoveries about this cell type (Acuna-Goycolea et al., 2008; Seabrook et al., 2013; Golding et al., 2014). The biggest advances involve their migration to dLGN, and the assembly of inhibitory circuits (Munsch et al., 2005; Seabrook et al., 2013; Golding et al., 2014). dLGN interneurons originate from the neuroepithelium of the third ventricle, and travel through ventral thalamus to arrive in dLGN (Golding et al., 2014). However, a recent report has challenged these findings, asserting that interneurons arise exclusively from the dorsal midbrain, and course rostrally before entering dLGN (Jager et al., 2016).

While their migratory path to dLGN is open to debate, their dispersion throughout the nucleus and the establishment of feedforward connections seems more firmly established (Sherman and Guillery, 2002; see chapter II). In part, these events depend on retinal signaling (Golding et al., 2014). Early postnatal optic nerve section models show an abnormal clustering of interneurons, and decreased inhibition in dLGN. However, what remains unanswered is whether their initial migration and targeting to dLGN also relies on retinal signaling or innervation. The molecular mechanism(s) underlying how retinal input guides interneuron migration is also unknown. Recent unpublished observations in the Fox lab suggest that fibroblast growth factor 15 (Fgf15) plays an important role.

Fgf15, a neurotrophic factor involved in GABAergic differentiation (Martinez-Ferre et al., 2016), is expressed in RGCs at ages when retinal axons innervate dLGN (Kurose et al., 2004). Preliminary data from Fox and colleagues show that in the absence of retinal input, there is a 3-fold reduction of Fgf15 in both dLGN and vLGN, suggesting this factor may provide a signal to help guide interneurons to dLGN.

To address these issues, we used the GAD67-GFP strain, mice that express green fluorescent protein (GFP) in thalamic interneurons, to visualize the location of interneurons as they make their way to dLGN. Moreover, by making biotinylated dextran amine (BDA) injections at perinatal ages into presumed sites of interneuron origin, we tracked the location of double-labeled GFP-containing cells, to trace the migratory path of dLGN interneurons. Secondly, we employed a loss-of-function approach by using a form of genetic deafferentation to evaluate if retinal signaling plays a role in the targeting of interneurons to dLGN. A genetic approach provides considerable advantages over postnatal manipulations such as optic nerve section or enucleation. Since the latter are done well after the time retinal axons innervate dLGN (Godement et al., 1984; Guido, 2008) and during the peak period of interneuron migration, it is difficult to rule out if results are caused by trauma or degeneration. By contrast, the math5$^{-/-}$ mouse, mutants that lack an optic nerve and central projections (Brown et al., 1998), provides a way to directly test the relationship between retinal axon innervation and dLGN development.

Finally, we began to explore the potential link between retinal signaling and Fgf15 during interneuron migration and distribution by utilizing the Fgf15 knockout mouse (Fgf15$^{-/-}$). Mutants show disruptions in the organization of thalamic progenitors (Martinez-Ferre et al., 2016), which allowed us to test how developmental processes such as interneuron migration are impacted by the loss of this neurotrophic factor.

Materials and Methods

Animals

All experiments were conducted in mice of either sex ranging in age between P0-P45. Three strains were used: GAD67-GFP (line G42; Jax stock no. 007677) established on a C57/B6 x CB6F1/J), math5$^{-/-}$ crossed onto GAD67·GFP, and Fgf15$^{-/-}$ mice crossed onto GAD67·GFP. The math5$^{-/-}$ strain was established on a mixed background of C57/B6 and 129/SvEv (Wang et al., 2001; El-Danaf et al., 2015), and Fgf15$^{-/-}$ mice were donated from the Mike Fox lab (VCU), derived from Dr. Steven Kliewer (University of Texas Southwestern) (Wright et al., 2004). All procedures were approved by the University of Louisville Institutional Animal Care and Use Committee.

Tissue harvest

Brain tissue was harvested from mice that were deeply anesthetized by hypothermia (<P5) or 4% isoflurane vapors (>P5). All animals were transcardially perfused with phosphate-buffered saline (PBS, 0.01 M phosphate buffer with 0.9% NaCl) followed by 4% paraformaldehyde (PFA) in 0.1 M phosphate buffer. Brains were excised and post-fixed overnight in 4% PFA, then transferred to PBS.

Interneuron imaging and analysis

Using a vibratome (Leica VT1200S), thalamic sections of 70 μm that included vLGN, dLGN, LPN, and VB were collected, mounted with Prolong Gold (with

12

DAPI; Invitrogen, catalog no. P36931), and coverslipped for confocal microscopy. Sections were imaged throughout the rostral-caudal extent of thalamus using a multi-photon laser scanning confocal microscope (Olympus, model no. FV1200BX61). A HeNe laser (488 nm) was used to excite GFP fluorescence and visualize interneurons under 10x (0.3 NA) or 20x (0.75 NA) objective lenses at a scanning resolution of 1600x1600 resolution. Optical slices were collected sequentially, with the optimal step size through the Z axis (8.51 μm, 10x; 1.26μm, 20x). Z-stacked datasets were uploaded into Imaris software (Bitplane, version 8.4.1) and ImageJ (version 1.50h, NIH) for analysis. DAPI was used to delineate the borders of thalamic nuclei, and we observed the migratory path of interneurons through thalamus.

To examine the number of interneurons in different thalamic nuclei, we obtained estimates of cell counts in dLGN, vLGN, LPN, and VB. For each nucleus, we utilized ImageJ to first outline (freehand selection tool) the region of interest. Using the Cell Counter tool, we counted and averaged the number of interneurons in 3 sections through the middle of the nucleus from 3 different mice at several different postnatal ages ranging from P0 to P45.

To determine the distribution of interneurons in dLGN and LPN, we divided each nucleus into "top" and "bottom" tiers. Three straight lines (Straight, Segmented tool) were drawn across the width of the nucleus: the bottom border, the widest point, and the top (Fig. 3A, 9A). The midpoints of each line were then connected. Using the cell counter, the total number of interneurons in each sector was calculated and used to generate a ratio: $\frac{\#\ of\ cells\ in\ top}{\#\ of\ cells\ in\ bottom}$

In order to examine interneurons density in dLGN, first we measured the area of dLGN (analyze tab) (μm^2) and calculated: ~~Total # of interneurons~~ / dLGN Area. To convert these values to whole numbers, we created a proportion to calculate values as a function of 2500 um2: total # of interneurons / dLGN Area = x / 2500 (Seabrook et al., 2013).

——————— ——

Biotinylated Dextran Amine (BDA) injections

To identify the migratory path of dLGN interneurons, intracranial unilateral injections of biotinylated dextran amine (BDA) were made in the superior colliculus (n = 7 mice) and along midline near the dorsal aspect of the third ventricle (V3) (n = 4 mice) at postnatal day zero (P0) in GAD67-GFP mice. Before injections, all animals were given Carprofen (5mg/kg), then deeply anesthetized by hypothermia. A glass pipette (20-40 μm tip diameter) connected to a picospritzer (General Valve Corporation) (1-2 μl, 2-4 pulses) containing a 5% solution of BDA (Invitrogen) in saline was lowered into V3 (from bregma: 3.75 mm posterior, 0.5 mm lateral, 2 mm ventral) or SC (from bregma: 4.09 posterior, 0.68 lateral, 1.7 ventral) (Atlas of the Developing Mouse Brain, Paxinos). After removal of glass pipette, scalp skin was sealed with tissue adhesive (*n*-butyl cyanoacrylate), and animals were placed on a heating pad until mobile. Carprofen was administered once every 12 hours for 24 hours, and we assessed and administered analgesic need for each animal up to 48 hours after surgery.

At P7, mice were perfused and brains excised as previously described. To visualize BDA-labeled cells, 40 μm sections were collected for streptavidin-546 (Invitrogen) immunohistochemistry. First, sections were placed in blocking

medium (0.3% Triton X-100 in filtered PBS) for 30 minutes, and incubated for 1

hour with SA-546 (1% SA546 in filtered PBS). Sections were washed 3 times for

15 minutes each in filtered PBS, and then mounted and coverslipped using

ProLong Gold mounting medium containing DAPI (Invitrogen, catalog no.

P36931) for confocal microscopy. To image BDA-labeled and double-labeled

interneurons, the lasers activating wavelengths 488nm (GFP) and 546 nm (BDA;

red) were included in imaging settings. Optical slices were collected sequentially

though the entire rostral-caudal extent of dLGN (~6 40 um sections) using the

"Line" mode to prevent channel bleed-through during acquisition.

Caspase-3 immunohistochemistry

To stain for cleaved caspase-3 (Cell Signaling Technology, product #9661), 40

μm sections were placed in blocking medium (10% normal goat serum (NGS)

and 0.3% Triton X-100 in filtered PBS) for 30 minutes, and then incubated

overnight (at least 18 hours) in primary antibody (1:400 caspase 3 and 1% NGS

in filtered PBS). The next day, treated sections were washed 3x in filtered PBS,

15 minutes each. All sections were incubated for 1 hour with the secondary

antibody (1:100 goat anti-rabbit AF546 (Invitrogen) and 1% NGS in filtered PBS).

Sections were washed 3 times (15 minutes each) before mounted and

coverslipped using ProLong Gold with DAPI. Sections from WT and math5^{-/-} were

imaged on the confocal using the 546 and 488 lasers to excite red, caspase-3

expressing neurons and GFP fluorescence, respectively. Sections were collected

sequentially using "Line" mode to avoid bleed-through with the 10x and 20x

lenses. For each case (n = 1-2 mice per age), 6-8 sections through the rostral-caudal extent of thalamus were imaged, allowing us to estimate the number of double-labeled (GFP+ and caspase-3+) interneurons at different ages.

Experimental design and statistical analysis

All statistical tests were conducted using Prism 7.0 (Graphpad Software, La Jolla, CA). A two-way ANOVA was used to examine age-related different within group (GAD67·GFP or math5$^{+/-}$ or Fgf15$^{+/-}$) and between groups (GAD67·GFP vs. math5$^{+/-}$; GAD67·GFP vs. Fgf15$^{+/-}$) across the various criteria for migration/distribution (i.e. total number of cells, area, ratio of cells, density, etc.). The *post-hoc* Holm-Sidak test was applied twice to allow for multiple comparisons within and between group across postnatal weeks. To compare the ratios of cells between dLGN and other thalamic nuclei in WT and math5$^{-/-}$ (Fig. 9), a Chi-Square analysis was performed.

Results

We investigated the migratory path of thalamic interneurons that are destined to populate the dorsal lateral geniculate nucleus (dLGN). To accomplish this, we utilized the GAD67-GFP mouse, a transgenic strain that expresses green fluorescent protein (GFP) in dLGN interneurons (Munsch et al., 2005; Seabrook et al., 2013; Golding et al., 2014; Leist et al., 2016). This allowed us to track their perinatal migration to dLGN, and assess how they enter and disperse themselves throughout the nucleus. Additionally, to examine whether retinal signaling influences migration, targeting, and distribution in dLGN, we employed a genetic form of retinal deafferentation by crossing the GAD67-GFP strain with the math5 null (math5$^{-/-}$) mouse.

Migratory path of interneurons in WT and math5$^{-/-}$ mice

Figure 1 reveals the migratory path of GFP-containing interneurons in the dorsal thalamus of GAD67·GFP (A) (i.e. WT) and GAD67 x math5$^{-/-}$ (B) (i.e. math5$^{-/-}$) mice. In both groups, interneurons followed a path that originates from the ventral wall of the third ventricle (see Fig. 1, P0). In WT, at perinatal ages neurons can be seen coursing the ventral border of the somatosensory ventrobasal (VB) complex, to then gather in the ventral lateral geniculate nucleus (vLGN). By P2, interneurons innervate the dLGN and occupy the region just beneath the optic tract, along the dorsolateral edge of the nucleus (see also Fig. 3). However, in math5$^{-/-}$, fewer interneurons were seen along this path and the trajectory, targeting, and dispersion of cells were disrupted. These observations are consistent with previous findings that show in WT mice, interneurons

17

destined for dLGN follow a ventrolateral stream from 3rd ventricle to travel

through thalamus before innervating dLGN, and that this migratory path is

disrupted by early postnatal optic nerve section. (Golding et al., 2014). However,

the presence of this ventrolateral thalamic stream has been challenged. A recent

report argues that the exclusive migratory path of interneurons originates from a

region in the dorsal midbrain. Ex-vivo time lapse imaging of a subset of

genetically labeled interneurons identified a presumptive stream originating in

superior colliculus (SC), migrating along a rostrolateral path through pretectum

before entering the dorsolateral edge of dLGN (Jager et al., 2016). To address

this discrepancy, we injected a neuronal marker, biotinylated dextran amine

(BDA), to label GFP-containing interneurons near the third ventricle (V3) and

superior colliculus (SC) of P0 GAD67 mice. This allowed us to examine the

location of labeled interneurons after the first postnatal week when migration is

complete (Golding et al., 2014). Following the injections, we conducted

streptavidin-546 immunohistochemistry to visualize and track BDA-labeled cells

(red), and assess whether interneurons doubled-labeled with GFP and BDA (see

Fig. 2) migrated into dLGN.

The top panels in Figure 2 show examples of BDA injections made near

V3 (left) or SC (right). The bottom panels show representative sections through

the middle of dLGN at P7 for three different cases. For injections near V3, in all 4

cases there were at least 1-3 double-labeled interneurons found in section

through dLGN (Fig. 2, bottom left). By contrast, in all 7 cases of SC injections, we

failed to detect any double-labeled interneurons in dLGN (Fig. 2, bottom right).

Taken together, our results are consistent with earlier reports showing that interneurons follow a ventral-dorsal pattern of migration from the neuroepithelium of V3 (Golding et al., 2014).

Number and distribution of interneurons in dLGN of WT and math5$^{-/-}$ mice

To determine how and when interneurons fully populate dLGN, we obtained estimates of their numbers and distribution throughout the nucleus at different ages for WT and math5$^{-/-}$ mice. Figure 3A displays representative coronal sections through WT dLGN at different postnatal ages between P0-P30. During the first week, we observed a rapid increase in the number of interneurons populating dLGN. Initially, interneurons clustered within the dorsolateral region of dLGN just beneath the optic tract, then gradually migrated in a ventral manner to become evenly distributed throughout the nucleus. However, as shown in Figure 3B, in math5$^{-/-}$ mice, far fewer interneurons were found in dLGN, and those that entered failed to disperse themselves, remaining clustered in the dorsolateral sector. These age-related changes in WT (black symbols), and the disruptions noted in math5$^{-/-}$ (red symbols) are summarized in Figure 4A·B.

Figure 4A plots the mean number of interneurons found in a section through the middle of dLGN as a function of age (n = 3 mice and 3 sections per age). For WT, between P0-P4, the mean number of neurons increased substantially (Fig. 4A) (Two-Way ANOVA, F$_{(9, 178)}$ = 198.2, p < 0.001; Sidak post-hoc test, all p values < 0.0001), and stabilized at P4 to approximately 110-120 cells per section. As noted in Figure 3, interneurons seem to follow a dorsal-to-ventral trajectory as they disperse themselves throughout dLGN. To track this

progression, for each section through dLGN, we divided the nucleus in half, and simply counted the number of cells in each tier to generate a top-to-bottom ratio (see Methods, Fig. 3, P7). The mean ratios in a section of dLGN plotted by postnatal age are shown in Figure 4B. Between P0-P3, there were twice as many interneurons in the top vs. bottom tier of dLGN (i.e., 2:1 ratio) (Two-Way ANOVA, $F_{(9, 181)}$ = 53.29, p < 0.001; Holm-Sidak post hoc test, all p values < 0.004). However, by P4, both tiers had equal numbers and a 1:1 ratio was maintained at all ages thereafter (p = 0.998). Taken together, these results indicate that interneuron migration to, and dispersion within dLGN are linked processes that are complete by P4.

As shown in Figure 4, math5$^{-/-}$ mice interneuron cell counts and distribution were altered. Between P0-7, the number of interneurons in dLGN increased significantly (Two-Way ANOVA, $F_{(9, 178)}$ = 198.2, p < 0.0001; Holm-Sidak post-hoc test, all p values < 0.0001), with mean values stabilizing after P7 (p = 0.904) to 50-70 interneurons per section (Fig. 4A) . During this time, math5$^{-/-}$ interneurons experienced significant changes in the way they arranged themselves within the nucleus (Fig. 4B) (Two-Way ANOVA, $F_{(9, 181)}$ = 53.29, p < 0.0001; Holm-Sidak post-hoc test, all p values < 0.0001). Between P0-P3, math5$^{-/-}$ showed ratios as high as 7:1 and 4:1. When interneuron distribution stabilized (p = 0.965) by the end of week 1, twice as many neurons were found in the top compared to the bottom of dLGN (i.e., 2:1).

Although math5$^{-/-}$ interneurons arrive and disperse within dLGN, comparisons with WT revealed a number of differences. At all ages after P4,

math5$^{-/-}$ mice contained significantly fewer dLGN interneurons (Fig. 4A) (Two-Way ANOVA, $F_{(1,178)}$ = 454.9, p < 0.001; Holm-Sidak *post-hoc* test, all p values < 0.0001). Moreover, at all ages there were significantly more interneurons occupying the superifical tiers of dLGN (Fig. 4B) (Two-Way ANOVA, $F_{(1, 181)}$ = 268, p < 0.001; Holm-Sidak *post-hoc* test, all p values < 0.0001). These results suggest that retinal innervation is needed for interneuron dispersion after arrival in dLGN.

Estimates of WT interneuron density, which take into account the age-related changes in dLGN size (Seabrook et al., 2013; El-Danaf et al., 2015), suggest that the overall size of dLGN is a regulating factor of interneuron number in dLGN. As shown in Figure 4C, there were significant age-related changes in interneuron density found in a section of dLGN (Two-Way ANOVA, $F_{(9,181)}$ = 59.99, p < 0.001; Holm-Sidak post-hoc test, all p values < 0.001) . During week 1, density increased from ~1 to 2-2.5 cells (per 2500 um^2 area), peaking at P5. Density then dropped back to 1 cell (per 2500 um^2) between P5 and P14 (Holm-Sidak post-hoc test, all p values < 0.004) and stabilized thereafter (p = 0.724). Figure 4D plots mean changes in dLGN size as a function of age, and reveals that dLGN area progressively increased during the first two postnatal weeks, as interneuron density fluctuated (Two-Way ANOVA, $F_{(9, 183)}$ = 213.544, p < 0.0001; Sidak post-hoc test, all p values < 0.0001). By P14, the area of dLGN reached its adult-like size (Fig. 4D, black) (p = 0.992), similar to when interneuron density stabilized (Fig. 4C, black).

In math5$^{-/-}$, density estimates revealed steady increases during the first postnatal week, as density increased from ~1 to 2 cells (per 2500 um^2 area) between P0 and P5 (Fig. 4C, red) Two-Way ANOVA, $F_{(9,181)}$ = 59.99, p < 0.0001; Holm-Sidak post-hoc test, all p values < 0.001). Density significantly decreased between P5-P7 (p < 0.0009) and stabilized thereafter to 1 cell (per 2500 um^2 area) (Holm-Sidak post-hoc, all p values > 0.720). The area of dLGN also increased significantly during week 1 (Fig. 4D) (Two-Way ANOVA $F_{(1,183)}$ = 213.544, p < 0.0001; Holm-Sidak post-hoc test, all p values < 0.0001), reaching an adult-like size by P7 (Holm-Sidak post-hoc test, all p values > 0.821). Interestingly, despite math5$^{-/-}$ dLGN containing fewer interneurons, density estimates were similar to WT (Two-Way ANOVA $F_{(1,181)}$ = 1.84, p = 0.177; all p values > 0.373) because of a ~2-fold reduction in dLGN area (Two-Way ANOVA, $F_{(1,183)}$ = 509.9, p < 0.001; Sidak post-hoc test, all p values < 0.0001) (El-Danaf et al., 2015). Taken together, these results suggest that the size of dLGN (Fig. 4C) regulates the number of interneurons present in the nucleus as a means to maintain constant density patterns.

There are two possible reasons for why there are fewer dLGN interneurons in math5$^{-/-}$ mice. First, mutants may undergo increased rates of apoptotic activity. Another may be that because of the interdependence between dLGN area and number of dLGN interneurons (Fig. 4C-D), interneurons are misrouted into nearby thalamic nuclei.

Apoptotic activity of interneurons in WT and math5$^{-/-}$ mice

To test for these possibilities, first we conducted caspase-3 immunohistochemistry on thalamic sections containing dLGN from WT and math5$^{-/-}$. Caspase-3, a protein responsible for disassembling cells into apoptotic bodies, serves as a reliable marker to visualize cells destined for cell death (McIlwain et al., 2013). Figure 5 demonstrates representative sections of dLGN that were processed for cleaved caspase-3 (red) from WT (A) and math5$^{-/-}$ (B) mice at young (P0-6), middle (P11-14) and adult (P24-25) ages (n = 1 mouse per age and 4 sections per age). In both cases, we detected neurons positive for cleaved caspase-3 in different thalamic nuclei, (see Fig. 5) but neither WT or math5$^{-/-}$ exhibited caspase-3+ dLGN interneurons at any age.

Number and distribution of interneurons in neighboring thalamic nuclei of WT and math5$^{-/-}$ mice

To assess whether interneurons are misrouted in the absence of retinal signaling, we obtained estimates of the number and distribution of interneurons in three other thalamic nuclei in math5$^{-/-}$ mice: ventrobasal complex (VB) and the ventral lateral geniculate nucleus (vLGN), both of which are part of the migratory stream, and the lateral posterior nucleus (LPN), a higher order visual nucleus that also contains interneurons.

First, we examined the ventrobasal complex (VB) which consists of the ventral posteromedial nucleus (VPM) and ventral posterolateral nucleus (VPL), that together serve to transfer nociceptive information to the primary somatosensory cortex (Welker, 1973; Harris and Hendrickson, 1987). Presently,

it is widely believed that the adult VB contains few, if any, interneurons (Harris and Hendrickson, 1987; Spreafico et al., 1994; Arcelli et al., 1997). However, as shown in Figure 6, many seem to pass through this region before arriving in dLGN.

Examples of cell count estimates in sections of VB in WT and age-matched math5$^{-/-}$ at different postnatal ages (P0-P30) (n = 3 animals and 3 sections per age) are shown in Figure 6A-B. Interestingly, in WT mice, interneurons were found throughout VB and were especially prevalent between P7-14. There was a significant increase (Two-Way ANOVA, $F_{(9, 134)}$ = 12.71, p < 0.001; all p values < 0.0001) in the number of interneurons within the first two weeks of postnatal life, with as many as 30 cells found in a given section through VB (Fig. 7C, black). After P11, the number of interneurons in a section decreased (Holm-Sidak *post-hoc* test, p = 0.004), but stabilized (Holm-Sidak *post-hoc* test, p = 0.998) to ~15-20 interneurons per section. These observations are consistent with other observations reveling a sparse population of interneurons residing in mouse VB. (Cavdar et al., 2014).

As shown in Figure 6B, math5$^{-/-}$ mice showed a similar trend for VB. During week 1, the number interneurons greatly increased from ~10 to ~45 per section. Values then decreased after P7, with sections averaging between 25-35 for the remaining ages (Holm-Sidak post-hoc test, all p values > 0.317). However, math5$^{-/-}$ mice exhibited far more interneurons in VB compared to WT (Fig. 6C, red) (Two-Way ANOVA, $F_{(1,134)}$ = 94.43; p < 0.0001), particularly between the ages P4-P21, where as many as 35-45 cells were found in a section

of VB (Holm-Sidak *post-hoc* test, $p < 0.001$). These results suggest that in the absence of retinal innervation, interneurons destined for dLGN are misrouted, resulting in increased numbers in VB.

We also examined the number of interneurons in another retino-recipient nucleus, the ventral lateral geniculate nucleus (vLGN). This structure plays an important role in visuomotor function and photo-entrainment of circadian rhythms (Brauer and Schober, 1982; Harrington, 1997), and is located just ventral to the dorsal dLGN. As shown in Figure 7A, a large population of GFP-positive interneurons reside primarily in the lateral magnocellular external sector of vLGN (Monavarfeshani et al., 2017).

Figure 7A-B provides representative coronal sections through vLGN at P0, P7, P14, and P21 for WT and math5$^{-/-}$ mice. As shown in the summary plot in Figure 7C, the mean number of vLGN interneurons in a section (n = 3 mice and 3 sections per age) significantly decreased (Two-Way ANOVA $F_{(3, 64)} = 114$, $p < 0.001$; all p values < 0.001) until P14 when values stabilized to ~75 cells (p values > 0.130). The number of vLGN cells in math5$^{-/-}$ followed a similar pattern, showing a decrease between P0 and P14 (Two-Way ANOVA $F_{(3,64)} = 114$, $p < 0.001$; all p values < 0.001), when cell count estimates then stabilized to ~25 neurons (p values > 0.058). However, at all ages, math5$^{-/-}$ mice maintained significantly fewer interneurons compared to WT (Fig. 7C, red) (Two-Way ANOVA, $F_{(1,64)} = 70.24$, $p < 0.001$ P0-P14; $p = 0.013$ P21). These results support the hypothesis that interneurons in math5$^{-/-}$ mice are misrouted, with many failing to arrive in vLGN and dLGN, remaining instead in VB.

We also examined the distribution of interneurons in LPN, a higher order thalamic nucleus that receives input from the superior colliculus, striate cortex, lateral extrastriate cortex, as well as the retina from melanopsin-expressing RGCs (Kaas and Lyon, 2007; Allen et al., 2016; Zhou et al., 2017). Though retino-LPN projections reduce to sparser levels in adult, it is possible that these retinal projections serve to coordinate the circuitry necessary for its visually-guided functions (Warner et al., 2012). This includes the arrangement of interneurons.

Figure 8A-B displays representative coronal sections through LPN at different postnatal ages (P0-P30) in WT and math5$^{-/-}$ mice. In a given section (n = 3 mice and 3 sections per age) we measured area of LPN, total number of interneurons, and their distribution. These findings are summarized in Figure 8C-E. In WT, within the first two weeks, the area of LPN significantly grew (Two-Way ANOVA, $F_{(8,108)}$ = 73.82, p < 0.0001, all p values < 0.001), until P11 when its size stabilized (Fig. 8C, red) (p = 0.965). Estimates based on the cell counts per section showed that total number of LPN interneurons significantly increased until P4 (Two-Way ANOVA, $F_{(8,108)}$ = 12.47, p < 0.0001, all p values < 0.001), when values stabilized thereafter to ~40 cells (Fig. 8D) (p = 0.998). During this time, estimates of the distribution of interneurons between the top and bottom tiers showed several significant changes. Between P0-P3, the majority of interneurons in a section populated the upper sector as much as 4:1 and 5:1 (Fig. 8E) (Two-Way ANOVA $F_{(8,108)}$ = 10.05, p < 0.05; Holm Sidak test, all p

values < 0.005). However, by P4 these ratios decreased and stabilized to a value of 2:1 (Holm-Sidak post-hoc test, p = 0.875).

As shown in Figure 8B, the LPN of math5$^{-/-}$ mice demonstrated similar age-related changes to WT. The size of the nucleus shows a steady increase until P11 (Fig. 8C, red) (Two-Way ANOVA, $F_{(8,108)}$ = 218.7, p < 0.0001, all p values < 0.001; (Holm-Sidak post-hoc test, p = 0.989). However, compared to WT, after week 1, LPN remained notably smaller at all ages (Fig. 8C) (Two-Way ANOVA, $F_{(1, 108)}$ = 73.82), p < 0.0001; all p values < 0.001). Estimates of the numbers of interneurons populating LPN in math5$^{-/-}$ mice revealed a steady increase from P0-4, then stabilized to values that averaged ~30 cells per section (Fig. 8D) (Two-Way ANOVA, $F_{(8,108)}$ = 12.47, p = 0.864). Additionally, between P0-P3, each section showed a large portion of interneurons occupying the top tiers compared to the bottom of LPN, having ratios as high as 8:1. At P4, LPN interneurons shifted to 5:1 ratio (Two-Way ANOVA, $F_{(8,108)}$ = 10.05, p < 0.001), and remained relatively steady thereafter (Fig. 8E) (Holm-Sidak post-hoc test, p = 0.728). However, compared to WT, math5$^{-/-}$ LPN displayed significantly fewer interneurons at ages P3, P11, and P14 (Fig. 8D) (Two-Way ANOVA, $F_{(1,108)}$ = 22.73, p = 0.0006; Holm-Sidak post-hoc test, P3 p = 0.049, P11 p = 0.003, P14 p = 0.006), and had a substantially higher proportion of cells residing in the top tier between P0 and P14 (Fig. 8E) (Two-Way ANOVA, $F_{(1,108)}$ = 73.57; p < 0.0001; Holm-Sidak post-hoc test, all p values < 0.04).

Taken together, our data suggests that the targeting of interneurons into visual thalamus is synchronized. Furthermore, the absence of retinal signaling

disrupts the targeting and organization of interneurons, as math5^{-/-} mice exhibited fewer and more clustered spacing. These disruptions are summarized in Fig 9A-B, which compares the number of interneurons residing in VB, vLGN, dLGN, and LPN for WT (A) and math5^{-/-} (B) mice. From these estimates, we generated ratios (at either P21 or 30) that compared the number of interneurons residing in dLGN, with those found in LPN, VB and vLGN (Fig. 9). Of these nuclei, the greatest shift was found in the proportion of interneurons in dLGN compared to VB, where WT mice displayed a 10:1 distribution (Fig. 9C, E), and math5^{-/-} mice showed a substantially smaller ratio, 2.5:1 (Fig. 9D, E) (Chi-square test 14.81, p = 0.0001). Taken together these data suggest that thalamic interneurons are misrouted and remain largely in VB, with many failing to complete their trajectory to dLGN.

Number and distribution of interneurons in dLGN, VB and vLGN in Fgf15^{-/-} mice

The results in math5^{-/-} mice suggest that migration and distribution of interneurons in dLGN relies on retinal signaling. However, the underlying molecular mechanism remains unclear. Here we explored Fgf15 as a potential candidate. This molecule is part of a large family of Fibroblast Growth Factors (FGFs) involved in cell differentiation, proliferation, and guidance (Borello et al., 2008; Hagemann and Scholpp, 2012; Martinez-Ferre et al., 2016). Indeed, Fgf15 is expressed in RGCs, the optic tract, retino-recipient nuclei, and ventricular zones (Gimeno et al., 2003; Kurose et al., 2004). Recent *in-situ* work from the Fox laboratory demonstrates a strong link between Fgf15 expression and retinal

signaling. Math5^{-/-} mice exhibit a 3-fold reduction in Fgf15 expression in dLGN

and vLGN at ages when interneuron migration is actively occurring (~P1-P3).

To explore this further, we employed a loss-of-function approach by utilizing the

Fgf15 knockout mouse (Fgf15^{-/-}), crossed onto the GAD67-GFP strain to

evaluate how the absence of Fgf15 influences interneuron migration to and

spacing within dLGN.

We estimated the size of dLGN, as well as the total number and

distribution of intrinsic interneurons within dLGN of Fgf15^{-/-} mice (n = 3 mice and 3

sections per age). Fig. 10A provides examples of coronal sections through the

dLGN of Fgf15^{-/-} and age-matched WT mice. Mutant mice displayed GFP-positive

interneurons at P7, P14, and P21. Interestingly, the area of dLGN was similar to

WT (Two-Way ANOVA $F_{(1,48)}$ = 12.76, p = 0.087, Holm-Sidak post-hoc test, all p

values > 0.343), with both showing a progressive increase in area between P7

and P14, before stabilizing to adult-like sizes by the end of the second postnatal

week (Fig. 10B) (WT, $F_{(2,48)}$, p = 0.599; Fgf15^{-/-}, $F_{(2,48)}$ = 12.75, p

= 0.066). However, at all ages, Fgf15^{-/-} mice exhibited significantly fewer number

of interneurons in a section of dLGN compared to WT (Fig. 10C, red) ($F_{(1,48)}$ =

38.8, p < 0.0001; Holm-Sidak *post-hoc* test, all p values < 0.006). Despite fewer

cells, interneurons were evenly dispersed at all ages (Fig. 10D, red) ($F_{(2,48)}$ =

3.77, p = 0.301; Holm-Sidak post-hoc test, all p values > 0.552), and with no

difference from WT ($F_{(1,48)}$ = 3.998, p = 0.512; Holm-Sidak post-hoc test, all p

values > 0.378). Thus, the absence of Fgf15 led to reduced numbers of

interneurons arriving in dLGN, but had no impact on the size of dLGN or the

manner by which interneurons arranged themselves within the nucleus. To determine if the loss of interneurons was due to misrouting, we examined the number of interneurons along the migratory of dLGN interneurons, including VB and vLGN.

Figure 11A shows examples of coronal sections through VB at different ages (P7, P14, P21) of WT and Fgf15$^{-/-}$ mice, and estimates of the number of interneurons in VB (n = 3 mice and 3 sections per age) are shown in Figure 11B. At ages P7 and P14, mutants displayed significantly more interneurons per section of VB compared to WT (Fig. 11B, red) ($F_{(1,48)}$ = 19.97, p < 0.001; P7, p < 0.0001; P14, p = 0.033). Figure 12A provides examples through vLGN with corresponding estimates of interneuron numbers for the two groups summarized in Figure 12B (n = 3 mice and 3 sections per age) at ages P7, P14, and P21. At all ages, Fgf15$^{-/-}$ showed significantly fewer vLGN interneurons (Fig. 12B, red) compared to WT ($F_{(2,72)}$ = 64.45, p < 0.0001; Holm-Sidak post-hoc test, p < 0.001).

Taken together these data suggest that loss of interneurons noted in dLGN of Fgf15 mutants is likely due to a misrouting of interneurons, with many failing to arrive in vLGN and instead settling in VB.
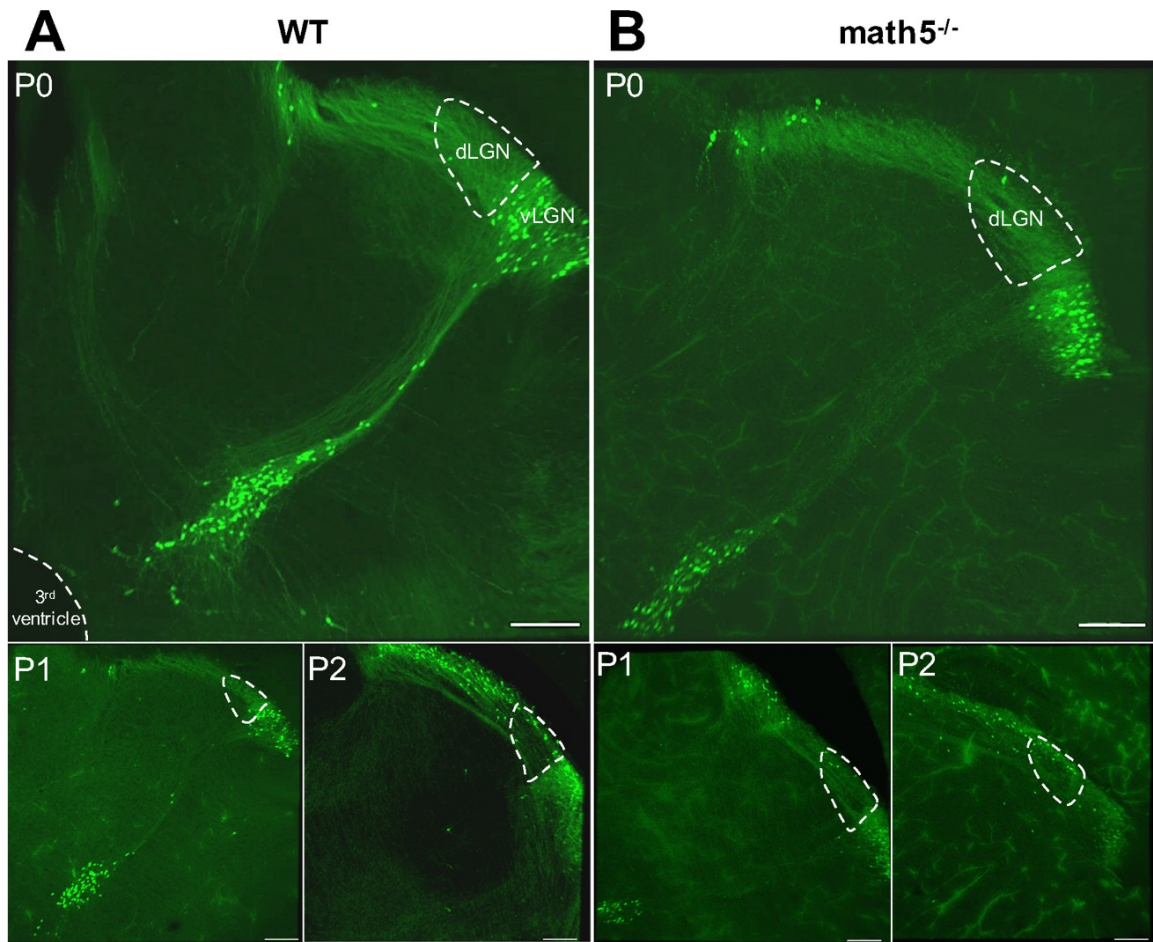
Figure 1: Green fluorescent protein (GFP) expressing interneurons in mouse thalamus of WT and math5$^{-/-}$ mice.

A: Representative coronal sections through the dorsal thalamus of GAD67-GFP (i.e. WT) mouse showing the migratory path of dLGN interneurons. **B**: Coronal sections through dorsal thalamus of GAD67 x math5$^{-/-}$ (i.e. math5$^{-/-}$) mouse depicting the trajectory, targeting, and distribution of dLGN interneurons at early ages. Scale bar: 150 μm.
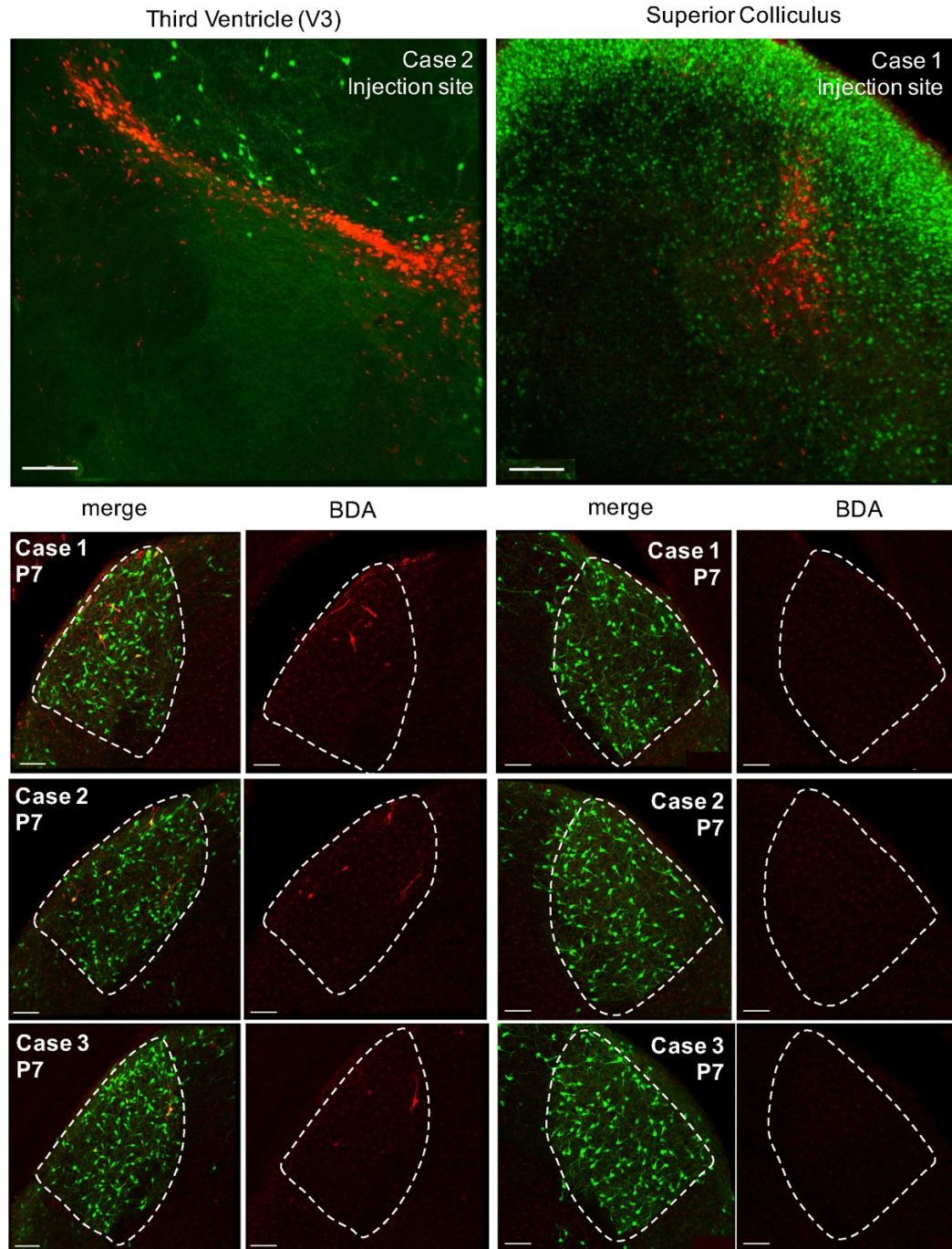
Figure 2: BDA injections near the third ventricle (V3) and in superior colliculus (SC) to target the presumed migratory streams of interneurons.

(Top): Representative coronal sections through dorsoventral thalamus (left) and SC (right) depicting the site of biotinylated dextran amine (BDA) injections in WT

mice at P0 (red; conjugated to Streptavidin-546) Scale bar = 150 μm. (Bottom):

Examples of sections through the middle of dLGN at P7 taken from 3 mice that

had either V3 (left) or SC (right) BDA injection. For each case, BDA-labeled

interneurons (left) and the corresponding GFP-labeled interneurons in dLGN are

shown. Double-labeled interneurons are illustrated (right) and found in dLGN of

mice after V3 injections. Scale bar = 70 μm.
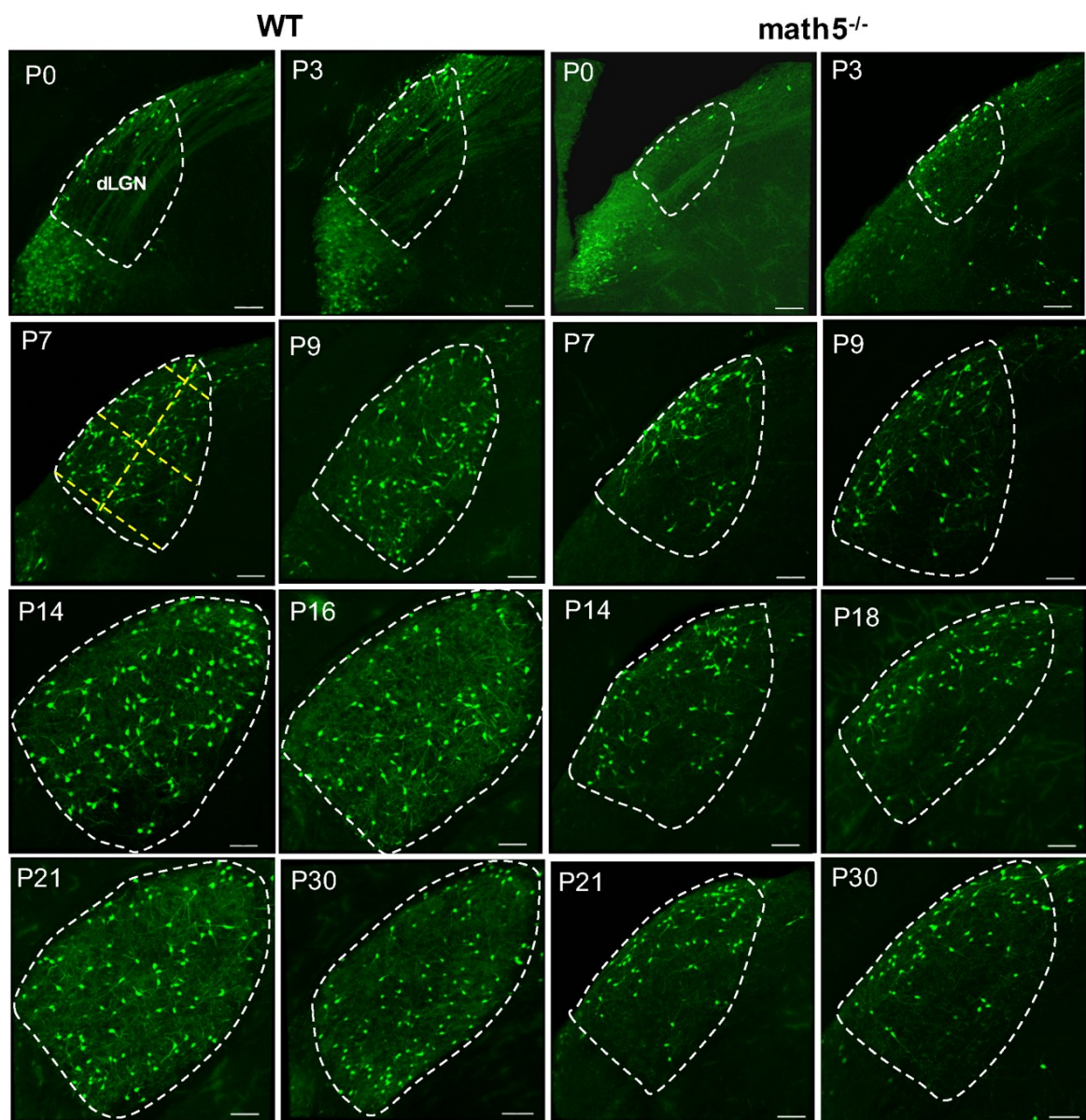
Figure 3: Pattern of interneuron migration and distribution in dLGN of WT and math5⁻/⁻ mice.

Representative coronal sections through dLGN in WT (left) and math5⁻/⁻ (right) depicting distribution and density of interneurons at different postnatal ages (P0,

P3, P7, P9, P14, P16, P18, P21, P30) (3 mice and 3 sections per age). In WT,

interneuron migration is complete by P4. In math5$^{-/-}$ mice,

There are fewer interneurons that reach dLGN, and those that do, appear

clustered in the dorsolateral region of dLGN. At P7 WT, dotted lines illustrate how

top and bottom tiers of dLGN were determined. Scale bar = 70 μm.
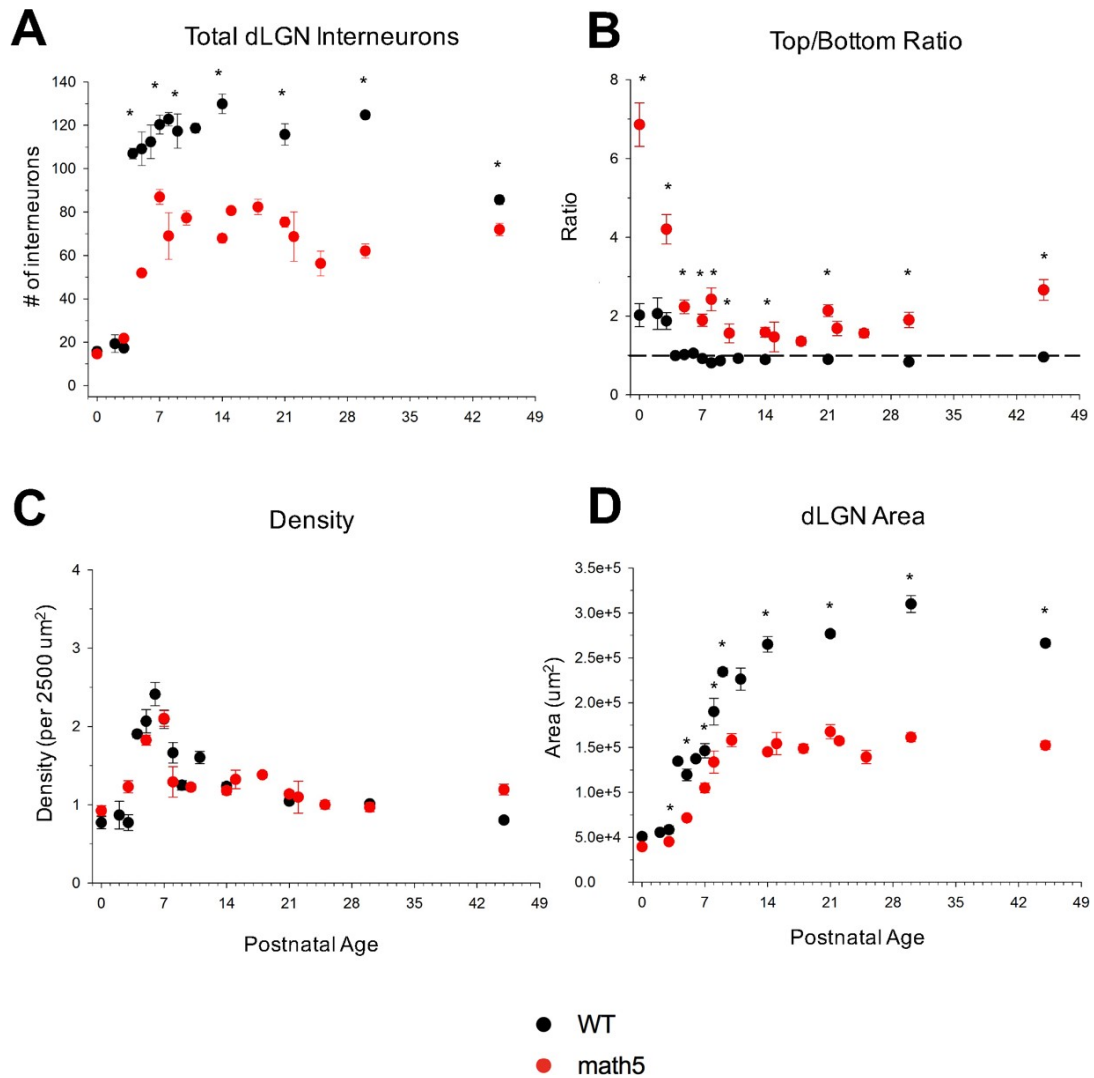
Figure 4: Estimates of the number of interneurons and their distribution in dLGN of WT and math5^{-/-} mice.

A-D: Summary plots depicting age-related changes in interneuron number **(A)**, distribution **(B)**, density **(C)** as well as estimates of the area of dLGN **(D)**. Each point represents mean values +/- SEMs for WT (black) and math5^{-/-} (red) as a function of postnatal age (3 mice and 3 sections per age). Asterisks (*) represent significance (<0.05) between WT and math5^{-/-}. Dotted line in **(B)** delineates equal distribution between top and bottom (1:1).
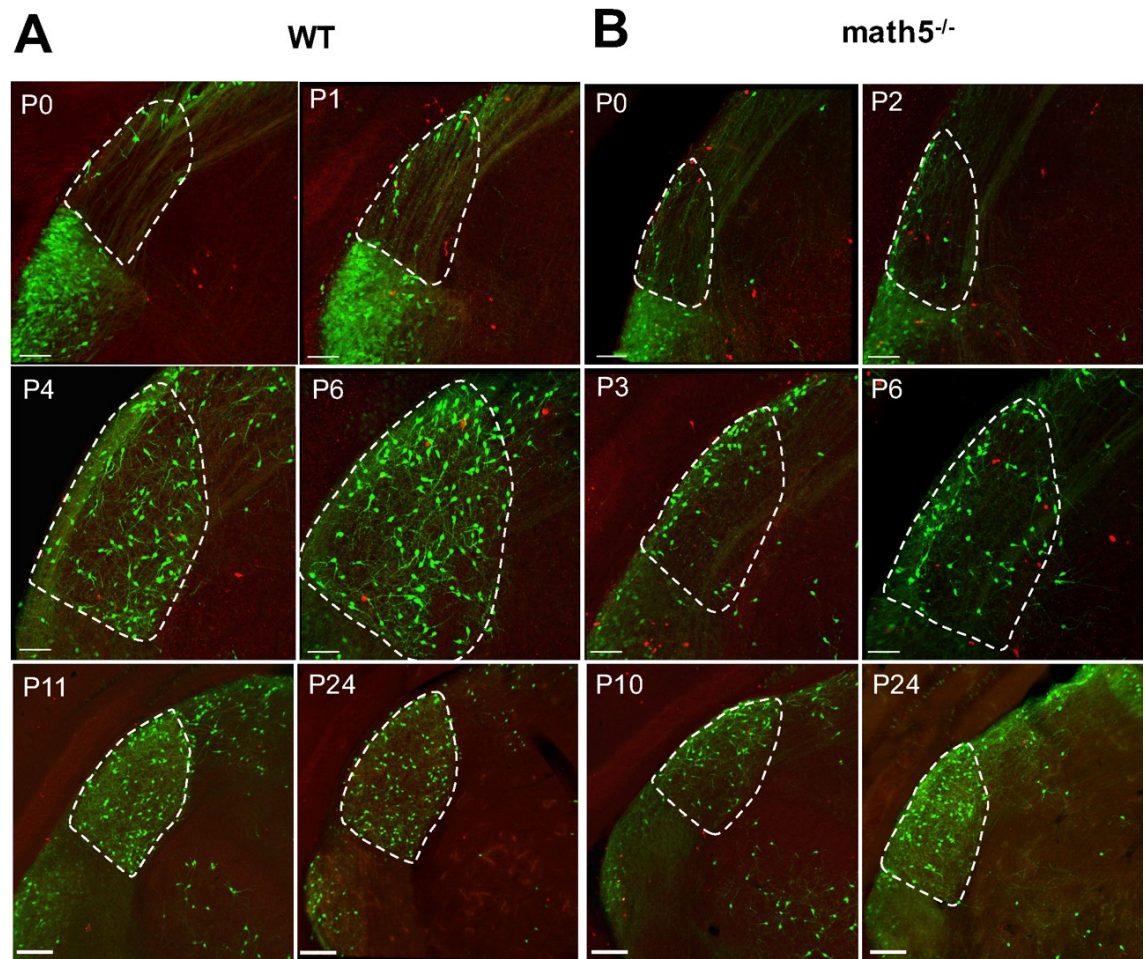
Figure 5: Observation of caspase-3 labeling in interneurons of WT and math5$^{-/-}$ mice.

A: Representative coronal sections through thalamus of WT mice at various postnatal ages (P0, P1, P4, P6, P11, P24) demonstrating the lack of caspase-3+ (red, Alexa-Fluor 546) interneurons in dLGN. **B**: Similarly, at all ages (P0, P2, P3, P6, P10, P24) math5$^{-/-}$ interneurons did not stain positive for caspase-3. For both groups and all ages: 1-2 animals, 5-7 sections per age. Scale bar = 70 μm, except for P10, P11, P24 = 150 μm.
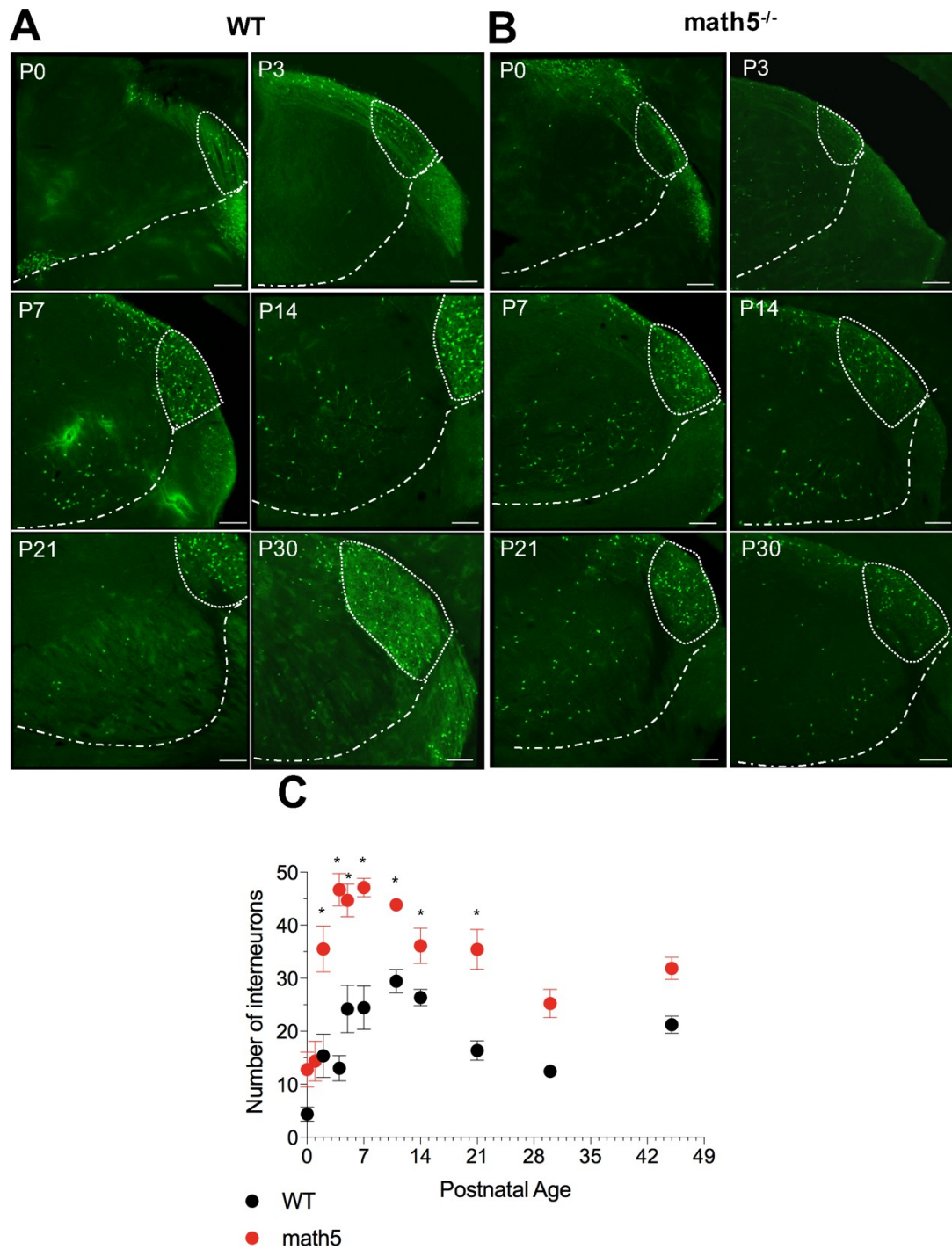
Figure 6: Pattern of interneuron migration in the ventrobasal complex (VB) of WT and math5^{-/-} mice. A: Representative coronal sections through VB in WT mice at different postnatal ages (P0, P3, P7, P14, P21, P30). Dotted line

delineates bottom boundary of VB; dLGN is outlined. B: Representative sections

of VB in age-matched math5$^{-/-}$ mice. **C**: Summary plot demonstrating age-related

changes in the number of VB interneurons in WT (black) and math5$^{-/-}$ (red) (3

mice and 3 sections per age) animals. At all ages, math5$^{-/-}$ mice show an

increased number of VB interneurons. Asterisks (*) represent significance (<0.05)

between WT and math5$^{-/-}$. Scale bar = 150 μm.
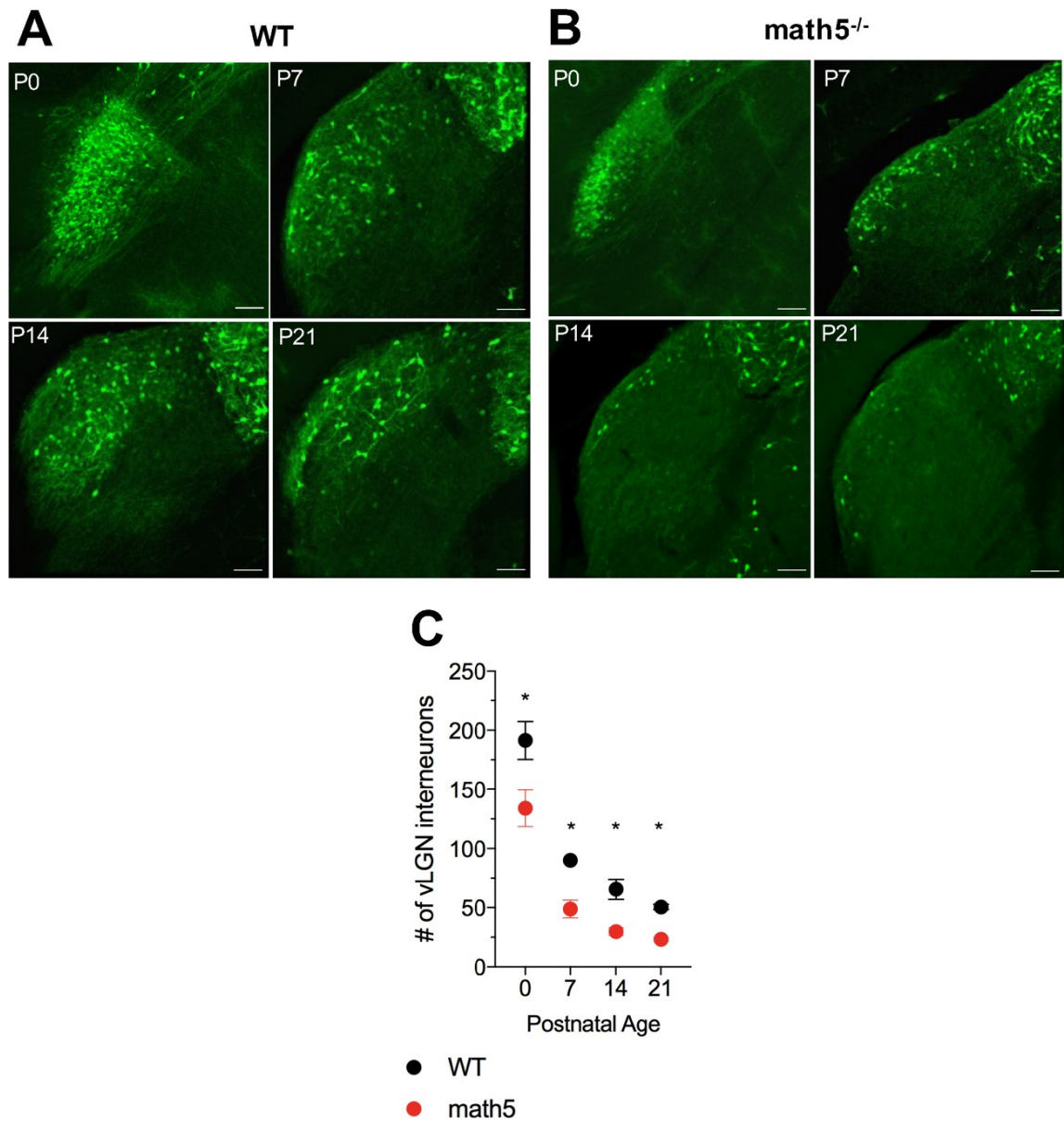
Figure 7: Interneuron distribution in vLGN of WT and math5^{-/-} mice.

A: Coronal sections through vLGN in WT at postnatal ages 7, 14, and 21. **B:** Representative coronal sections through vLGN in age-matched math5^{-/-} mice. **C:** Scatter plot displaying age-related changes in number of interneurons in WT (black) and math5^{-/-} (red) (3 mice and 3 sections per age). At all ages, math5^{-/-}

exhibit fewer interneurons. Asterisks (*) represent significance (<0.05) between

WT and math5$^{-/-}$. Scale bar = 70 μm.
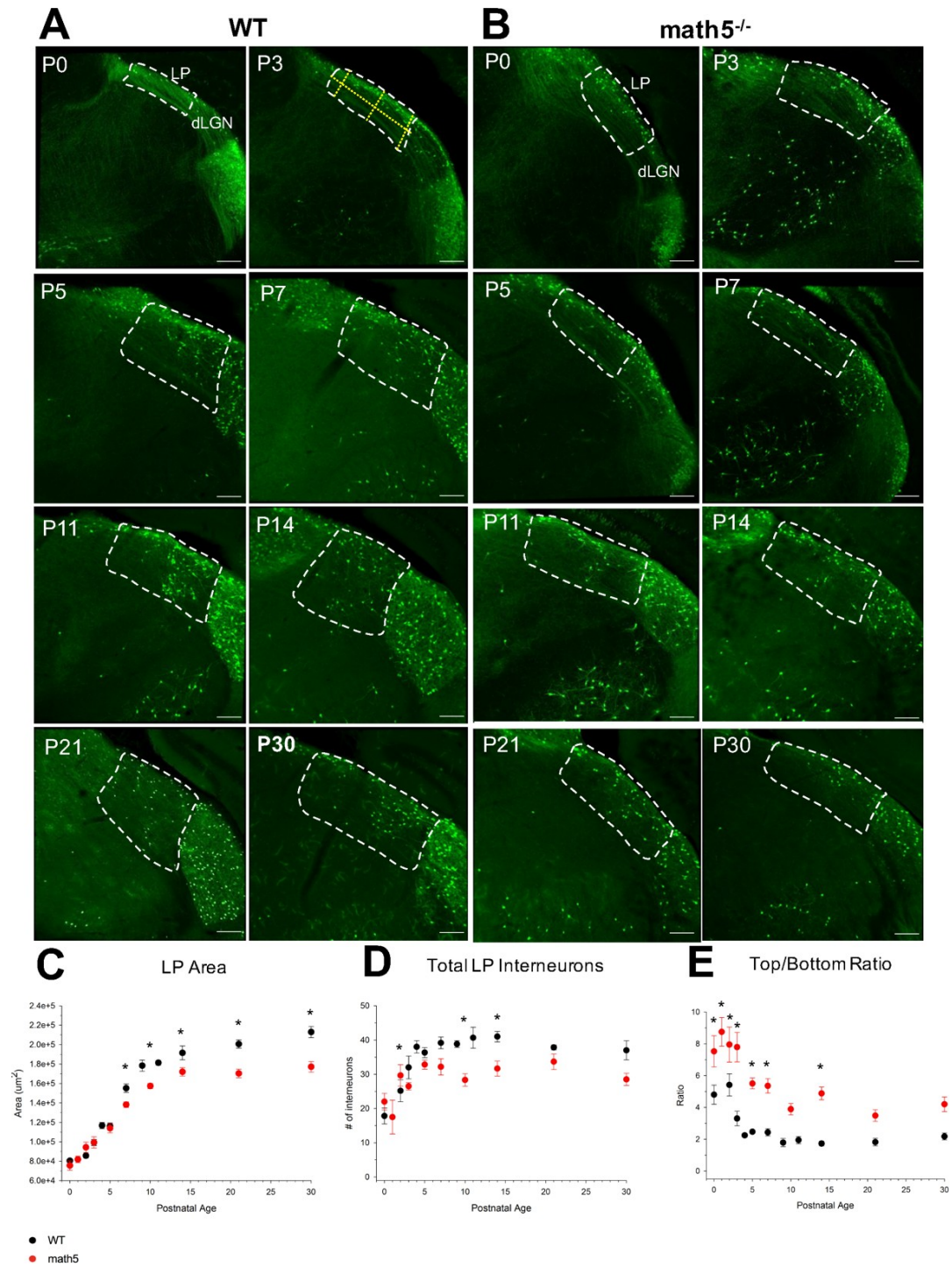
Figure 8: Estimates of the number and distribution of lateral posterior nucleus (LPN) interneurons. A: Example coronal sections through middle thalamus in WT, demonstrating number and distribution of cells in LPN (outlined)

at various postnatal ages (P0, P3, P5, P7, P11, P14, P21, P30). At early ages,

LPN interneurons occupy the dorsolateral sector before distributing ventrally. **B**:

Representative sections through thalamus in math5$^{-/-}$, mice showing altered

interneuron distribution in LPN at different postnatal ages (P0, P3, P5, P7, P11,

P14, P21, P30). **C-E**: Summary scatter plots demonstrating the age-related

changes in LPN area **(C)**, number of interneurons **(D)**, and ratio between cells in

the top and bottom sectors **(E)** in WT (black) and math5$^{-/-}$ (red) (3 mice and 3

sections per age). Overall, math5$^{-/-}$ exhibited reduced number of LPN

interneurons, and more cells clustered in the top sector of LPN compared to WT.

Asterisks (*) represent significance (<0.05) between WT and math5$^{-/-}$. Scale bar

= 70 μm.
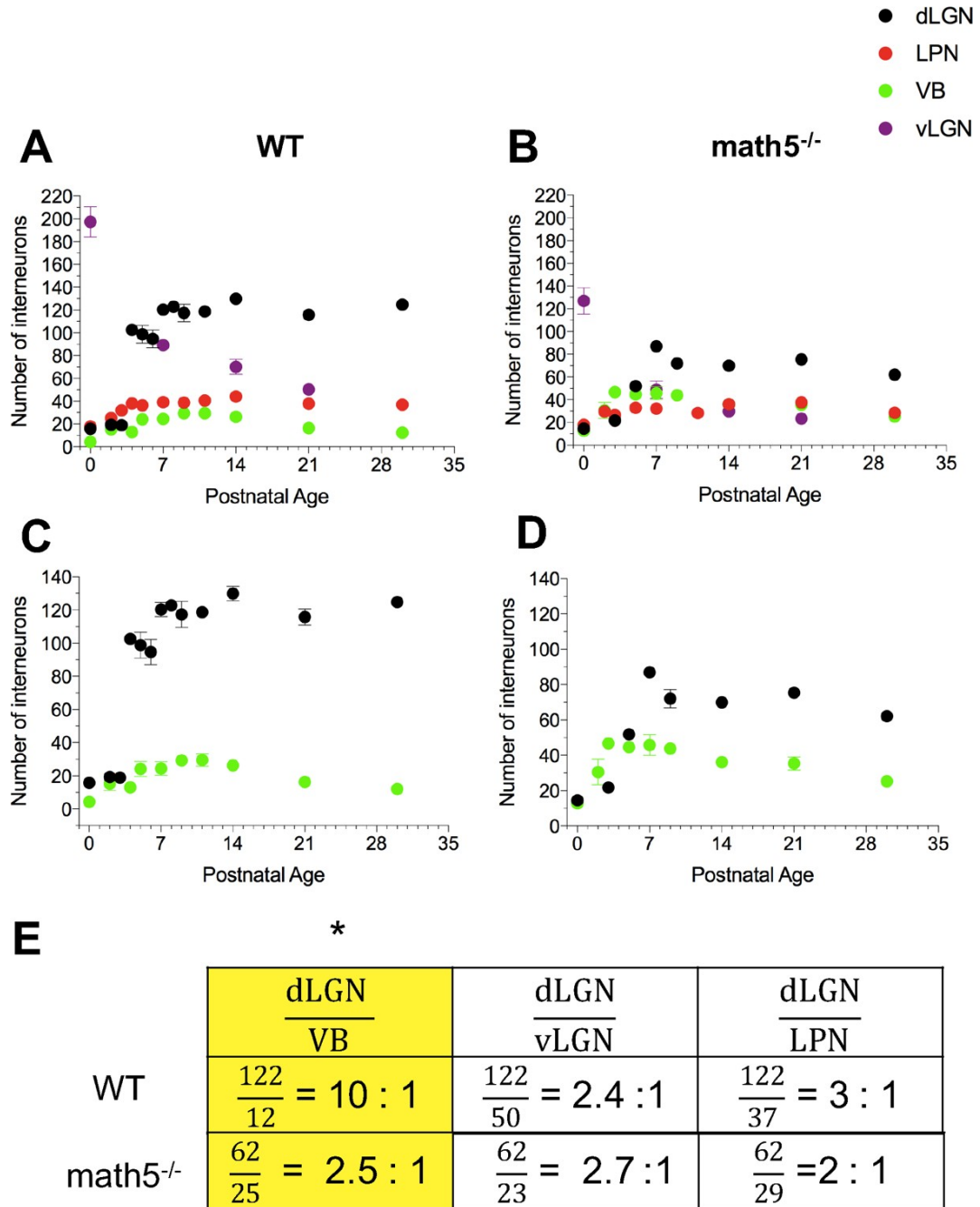
Figure 9: Organization of thalamic interneurons in WT and math5^{-/-} mice. A-B: Scatter plots summarizing changes in interneuron number across different thalamic nuclei and at postnatal ages ranging from P0-P30: dLGN (black), LPN (red), VB (green), and vLGN (purple) in WT **(A)** and math5^{-/-} **(B)** mice (3 mice

and 3 sections per age). Mutants show disruptions in total number and organization of thalamic interneurons. **C-D:** Same plots as shown in A-B, but only showing estimates from dLGN (black) and VB (green). **E:** Summary table demonstrating the discrepancy in interneuron number between dLGN and surrounding thalamic nuclei at an example age, P30 (VB, LPN) and P21 (vLGN). The yellow column and asterisk (*) highlights how the largest difference in interneuron number was between dLGN and VB (p = 0.0001).
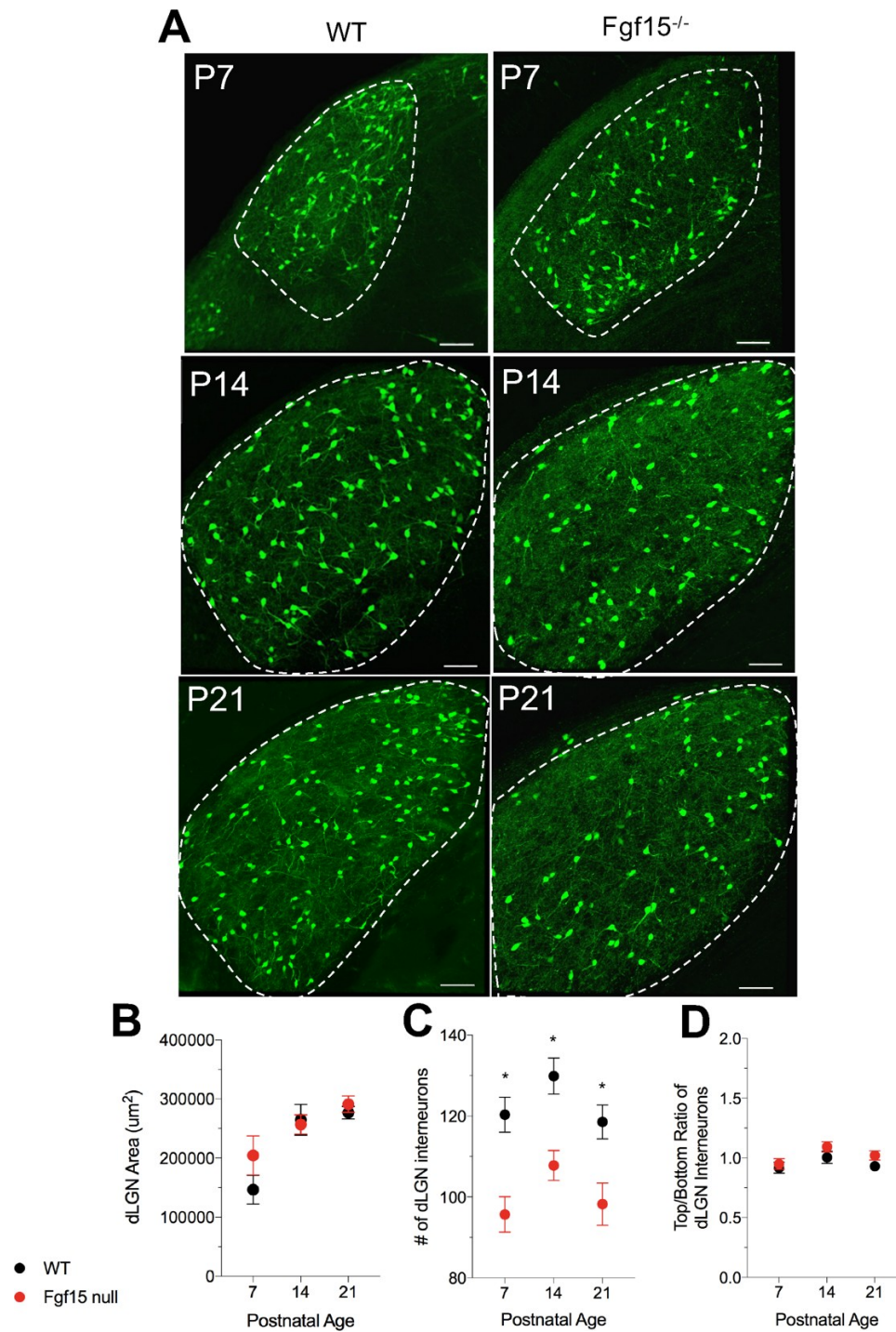
Figure 10: Interneuron number and dispersion in WT and Fgf15$^{-/-}$ mice.

A·B: Representative coronal examples through dLGN of WT (left) and Fgf15$^{-/-}$

(right) mice at postnatal ages 7, 14, and 21 (3 mice and 3 sections per age). **B-D:**

Scatter plots demonstrating age-related changes in area **(B)**, number **(C)**, and distribution **(D)** of interneurons in WT (black) and Fgf15$^{-/-}$ (red). Each point represents mean values +/- SEMs arranged by postnatal day (3 mice and 3 sections per age). **B:** Both WT and Fgf15$^{-/-}$ show similar area measurements **C:** At all ages, Fgf15$^{-/-}$ displayed decreased number of cells. **D:** However, interneurons in Fgf15$^{-/-}$ mice maintained an even distribution at all ages, similar to WT. Asterisks (*) represent significance (<0.05) between WT and Fgf15$^{-/-}$. Scale bar = 70 μm.
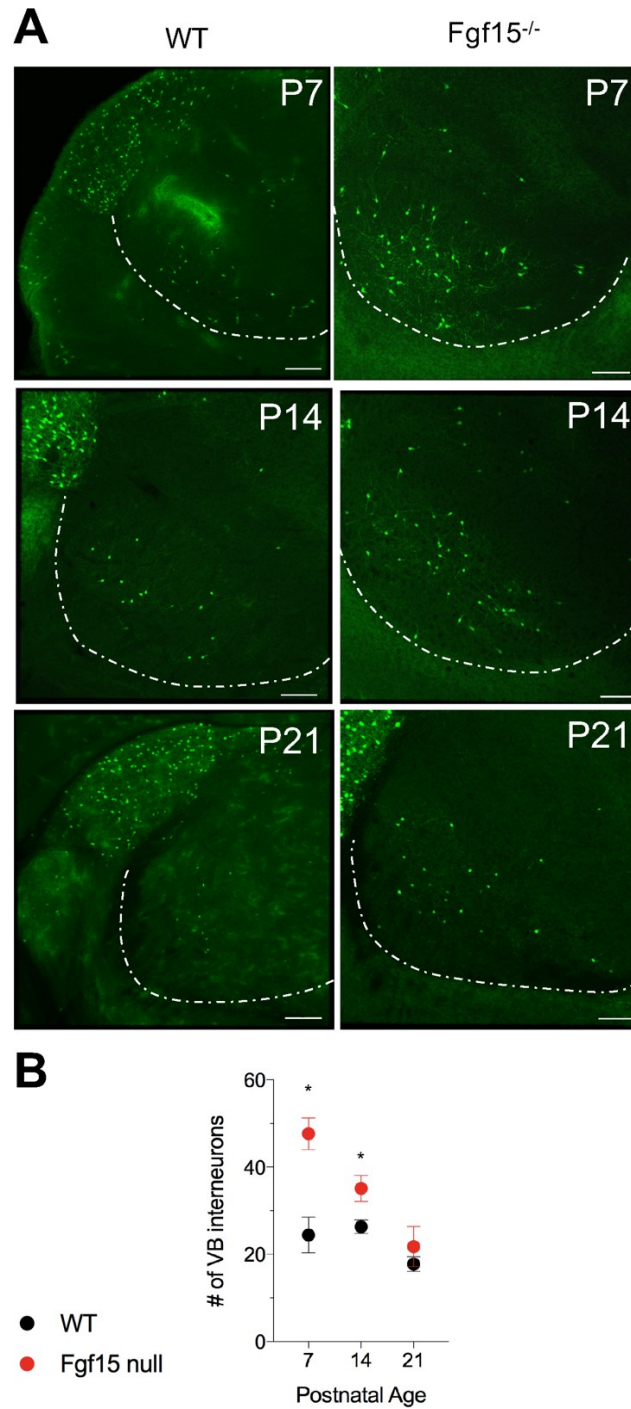
Figure 11: Estimates of the number of VB interneurons in Fgf15$^{-/-}$ mice.

A: Examples of coronal sections through thalamus showing number of VB interneurons in WT (left) and Fgf15$^{-/-}$ (right) at ages P7, P14, and P21. **B:** Scatter

plot displaying age-related changes in interneuron number in WT (black) and

Fgf15$^{-/-}$ (red) (3 mice, 3 sections per age). Fgf15$^{-/-}$ mice exhibited increased

number of neurons in VB, particularly at P7 and P14. Asterisks (*) represent

significance (<0.05) between WT and Fgf15$^{-/-}$. Scale bar = 150 μm.
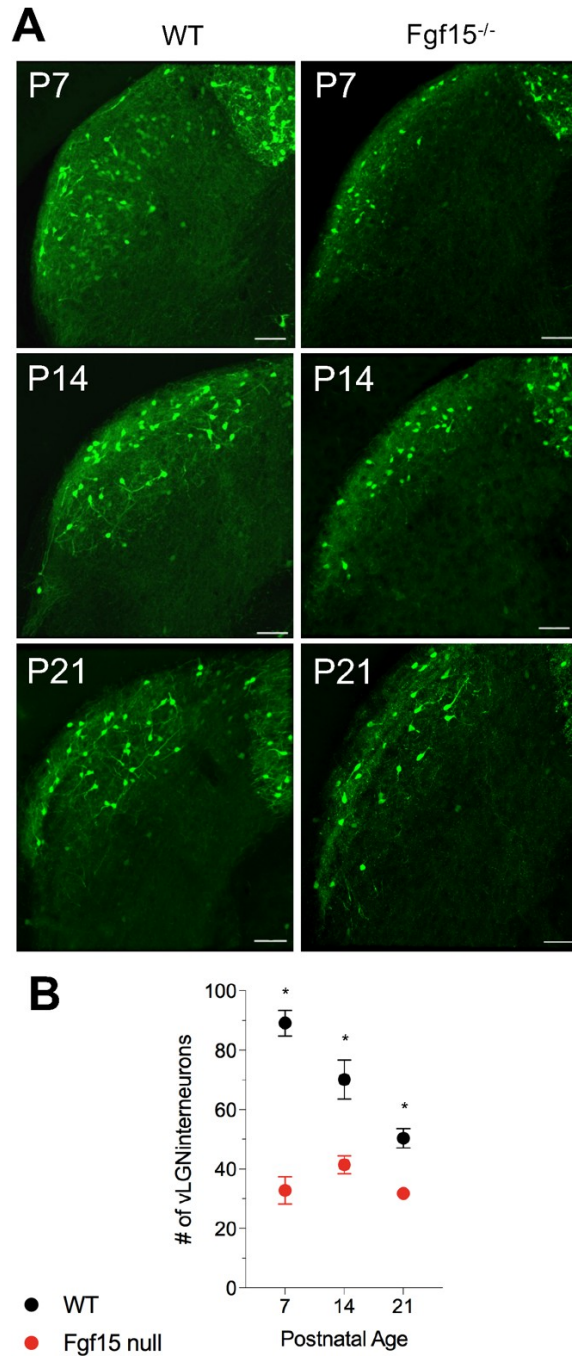
Figure 12: Fewer vLGN interneurons in Fgf15$^{-/-}$ mice.

A: Representative examples of the number of intrinsic interneurons in vLGN in WT (left) and Fgf15$^{-/-}$ (right) at ages P7, P14, and P21. **B:** Summary plot

depicting changes in vLGN interneuron number in WT (black) and Fgf15$^{-/-}$ (red)

(3 mice and 3 sections per age). At all ages, Fgf15$^{-/-}$ mice displayed fewer

interneurons than WT counterparts. Asterisks (*) represent significance (<0.05)

between WT and Fgf15$^{-/-}$. Scale bar = 70 μm.

Discussion

Our studies provide new insight about the migration, targeting, and dispersion of thalamic interneurons to, and within dLGN. Tracing studies with biotinylated dextran amine (BDA) injections confirm that dLGN interneurons follow a migratory path originating from the third ventricle (V3), and course through thalamus to gather in vLGN prior to their arrival in dLGN. We found that when interneurons were labeled with BDA at P0 in and around the midline of V3, they were distributed throughout dLGN at postnatal day 7. These findings are consistent with a previous study that showed dLGN interneurons follow a ventro-lateral stream from the neuroepithelium of V3, through VB and vLGN, before arriving to dLGN (Golding et al., 2014). This trajectory for interneurons has been challenged by a recent report that claims the exclusive source of dLGN interneurons is the midbrain structure superior colliculus (SC), that traverse in a rostral manner through pre-tectum to dLGN (Jager et al., 2016). However, we failed to identify such a path; BDA injections into SC at P0 did not reveal labeled interneurons in dLGN. One reason for such discrepancy may be due to the timing of injections, which were designed to focus on early postnatal migration, whereas the presumed rostral stream from SC involved perinatal ages (Jager et al., 2016). As a consequence, the timing of our early postnatal injections (P0) may have simply missed the time-frame when the bulk of migration along this path occurred. Thus, it is possible that there are two sources of interneurons, with two streams travelling in different directions and arriving in dLGN at successive times. The first migratory stream may occur largely at late embryonic ages and

includes interneurons traveling rostrally from SC. The second begins postnatally

with interneurons taking a ventro-lateral path through thalamus to dLGN.

Our experiments in WT mice reveal that dLGN interneurons first arrive in

the dorsolateral region of the nucleus just beneath the optic tract, then traverse

ventrally to become evenly dispersed by postnatal day 4. This progression is

similar to what others observe (Golding et al., 2014), but our analysis also

showed that migration to and dispersion within dLGN is complete earlier than

previously recognized. Moreover, work in math5^{-/-} reveal that fewer interneurons

migrate to dLGN, and those that do arrive remain clustered in the dorsolateral

sector. These results suggest that retinal signaling plays an important role in the

migration and dispersion of interneurons. This abnormal clustering associated

with math5^{-/-} is consistent with a previous report showing that after early

postnatal optic nerve section, interneurons fail to disperse evenly throughout

dLGN, and instead collect along the dorsolateral border (Golding et al., 2014).

However, our data reveals that retinal innervation also influences the targeting

and migration of interneurons to dLGN. Estimates reveal a ~50% reduction in the

number of interneurons present in dLGN in math5^{-/-} mice compared to WT.

Interestingly, despite these reduced numbers, the density of interneurons in

dLGN of math5^{-/-} mice is similar to WT. The similarity in density between WT and

these mutants is likely related to the highly reduced size of dLGN noted in math5^{-/-} mice (El-Danaf et al., 2015). Indeed, we found math5^{-/-} mice exhibit a ~2-fold

decrease in dLGN area compared to WT (Fig. 4D). Thus, it appears that the

overall size of dLGN is a major determinant of the total number of interneurons

residing in dLGN. Such a relationship is found in other brain structures such as the hippocampus, where studies have shown that a reduction in size of the CA1 region brought about by degeneration/aging, leads to substantially fewer neurons (Simic et al., 1997; Harding et al., 1998).

Although the density is the same, there are still far fewer interneurons in dLGN of math5$^{-/-}$ mice. To account for this loss, we explored whether this was a result of increased apoptotic activity, or the misrouting of migrating interneurons to other nearby nuclei. Caspase-3 labeling in math5$^{-/-}$ showed no evidence of postnatal interneuron cell death either in dLGN, or other thalamic and midbrain nuclei. Instead, estimates of interneuron numbers in nearby thalamic nuclei suggest that the absence of retinal input associated with math5$^{-/-}$ mice, leads to misrouting of interneurons destined for dLGN. In these mice, VB contained far more interneurons compared to WT (Fig. 6,9). Normally, the ratio of interneurons between dLGN vs. VB is 10:1, whereas in math5$^{-/-}$ mice, this value becomes 2.5:1 (Fig. 9E). In fact, when comparing the proportion of interneurons between dLGN and the surrounding nuclei, only VB was significantly different between WT and math5$^{-/-}$ (Fig. 9E). Taken together, these results support the hypothesis that the absence of retinal input disrupts the migration and targeting of dLGN interneurons at the level of VB. Neurons are misrouted and fail to reach their first destination (i.e. vLGN) prior to arrival in dLGN.

We also note that the absence of retinal signaling disrupted the number and pattern of interneurons in the lateral posterior nucleus (LPN). Similar to our results in dLGN of math5$^{-/-}$ mice, LPN showed fewer interneurons that were

54

clustered along the dorsolateral border. This structure is a higher-order visual

thalamic nucleus that receives its primary, excitatory drive from cortical layer V

(Roth et al., 2016; Zhou et al., 2017). Nonetheless, the link between retinal

signaling and interneuron fate likely exists given that LPN receives direct retinal

innervation from a subset of RGCs. A recent in-vivo study indicates that at least

25 percent of all LPN neurons can be driven by their retinal input (Allen et al.,

2016). Moreover, the density of retinal innervation is particularly high at early

postnatal ages (Warner et al., 2012), the time when interneurons are actively

migrating to their respective nuclei. While little is known about the migratory path

of interneurons destined to reside in LPN, our results in math5$^{-/-}$ suggest that

retinal signaling plays a role in their targeting and dispersion.

Finally, to address the underlying molecular mechanism for how retinal

signaling regulates interneuron migration and dispersion within dLGN, we

explored the role of the neurotrophic factor Fgf15. This signaling protein is a

member of the Fibroblast Growth Factor (FGF) family, known to play a role in

embryogenesis, cellular proliferation, and migration (Ornitz and Itoh, 2015).

Fgf15 in particular is involved in GABAergic neuron differentiation and

proliferation, operating through endocrine, paracrine, and autocrine signaling

pathways ((Borello et al., 2008; Ornitz and Itoh, 2015; Martinez-Ferre et al.,

2016). Moreover, Fgf15 is regulated by Otx2 expression, a transcription factor

implicated in directing interneuron migratory streams throughout many

subcortical structures (Vue et al., 2007; Golding et al., 2014). Previous studies

have also shown that Fgf15 is present within the neuroepithelium of the third

ventricle, the optic tract, as well as retino-recipient nuclei such as vLGN and dLGN (Gimeno et al., 2003). In fact, recent evidence from the Fox lab utilized in-situ, microarray, and quantitative-PCR to reveal that Fgf15 is expressed transiently at early postnatal ages, during the period of active interneuron migration (~P1-3). Most importantly, the Fox lab demonstrates that Fgf15 expression is linked to retinal innervation. In math5$^{-/-}$ mice, microarray and RNA-seq analysis showed a 3-fold decrease in Fgf15 expression within vLGN and dLGN compared to WT (Fox lab, unpublished observations).

Our experiments in Fgf15$^{-/-}$ mice seem to support the link between retinal innervation and Fgf15, as the number of interneurons in dLGN and vLGN were markedly decreased compared to WT (Fig.10, 12). Indeed, much like math5$^{-/-}$ mice, more neurons were found in VB (Fig. 11), suggesting that the migratory path of dLGN interneurons was disrupted in Fgf15$^{-/-}$ mice. Given that the loss of retinal axon innervation leads to decreased Fgf15 within the LGN complex (Fox lab, unpublished observation), these results indicate that the misrouting of dLGN interneurons is brought about by the loss of Fgf15. While both Fgf15 and math5$^{-/-}$ mice show fewer interneurons in dLGN, the losses were more severe in math5$^{-/-}$. These comparisons suggest that Fgf15 is a contributing factor, but not the exclusive one. It is likely that retinal signaling provides trophic support that influences the overall growth of dLGN, and the maturation of its neuronal components (El-Danaf et al., 2015; see Chapter II).

It is also important to note that while there were fewer interneurons within dLGN of Fgf15 mice, their dispersion within the nucleus was similar to WT (Fig.

10 C-D). These findings imply that Fgf15 plays a distinct role during interneuron migration, regulating their targeting and arrival but not dispersion. Thus, our data suggests that retinal signaling supports two molecular mechanisms, one for interneuron targeting and migration to dLGN (i.e. Fgf15 pathway), and the other within the nucleus that regulates their dispersion. Presently, we are exploring whether Down Syndrome Cell Adhesion Molecule (DSCAM) is involved in the spacing of interneurons within dLGN. This gene is expressed in several retinal cell types, and is required for a number of developmental processes including dendritic stratification, laminar patterning, and neuronal spacing (Fuerst et al., 2008; Yamagata and Sanes, 2008; Fuerst et al., 2012). Notably, DSCAM functions as a repulsive signal for proper neuronal spacing, and its loss leads to disruptions in the mosaic patterning of different retinal cell types (Fuerst et al., 2012). Additionally, a recent report showed that DSCAM is needed for proper segregation of eye-specific retinal terminal domains (Blank et al., 2011), and in WT, this gene is expressed along retinal axons that project to dLGN (Fuerst lab, unpublished observations). Thus, its loss in math5$^{-/-}$ mice may lead to abnormal dispersion of interneurons within dLGN.

Taken together, our results demonstrate the first comprehensive analysis of interneuron development, and shed light on the potential mechanisms that regulate the migration and dispersion of interneurons destined for dLGN. While retinal signaling plays an important role, it is clear that a number of molecules are affected, and that each may control a distinct aspect of interneuron targeting, migration, and dispersion.

CHAPTER II

DEVELOPMENTAL REMODELING OF THALAMIC INTERNEURONS

REQUIRES RETINAL SIGNALING

Introduction

The dorsal lateral geniculate nucleus (dLGN) of the mouse has become the

leading model system to understand many aspects of thalamic circuit

development (Huberman et al., 2008; Hong and Chen, 2011; Seabrook et al.,

2017; Guido, 2018). The advance of sophisticated genetic tools and widespread

use of genetically modified mouse strains permit remarkable experimental

access to study how specific cell types and circuits are established during early

postnatal life. However, our understanding of thalamic circuit development has

been largely limited to thalamocortical neurons, which serve as the exclusive

relay of retinal information to the visual cortex. These neurons undergo

substantial remodeling during the first few postnatal weeks, developing complex

and stereotypic dendritic architecture that defines their cell class specificity

(Krahe et al., 2011; El-Danaf et al., 2015). Such growth is accompanied by the

synaptic pruning of retinal connections whereby the number of functional inputs

onto dLGN relay neurons are greatly reduced (Chen and Regehr, 2000; Jaubert-

Miazza et al., 2005; Cheadle et al., 2018; Tschetter et al., 2018). Many of these

changes rely on retinal signaling. For example, the elimination of retinal input to dLGN leads to dystrophic dendritic growth (El-Danaf et al., 2015), and the blockade of early retinal activity results in synaptic weakening and a failure to prune excess retinal inputs onto developing dLGN relay neurons (Hooks and Chen, 2006)

By comparison, our knowledge about the development of the other dLGN cell type, intrinsic interneurons, remains rudimentary. These local circuit neurons which receive retinal input comprise <10% of total dLGN cell population (Evangelio et al., 2018). Despite their small numbers, they play a key role in retinogeniculate signal transmission by sharpening the spatio-temporal receptive field structure of dLGN relay neurons through a feedforward inhibitory circuit (Cox and Sherman, 2000; Bickford et al., 2010; Hirsch et al., 2015).

The recent utilization of the GAD67-GFP transgenic strain, which expresses green fluorescent protein (GFP) in dLGN interneurons, has led to a number of important discoveries about their genesis, migration, and assembly of inhibitory synaptic connections (Seabrook et al., 2013; Golding et al., 2014; Jager et al., 2016). Thalamic interneurons migrate to dLGN at perinatal ages, distributing themselves evenly throughout the nucleus by the end of the first postnatal week (Golding et al., 2014; Jager et al., 2016; see Chapter I). While interneurons receive retinal input at early postnatal ages, the formation of inhibitory connections occurs much later, well after the maturation of dLGN relay neurons and the initial phase of retinogeniculate synapse remodeling (Bickford et al., 2010; Seabrook et al., 2013). What is lacking is an understanding about how

these milestones relate to the morphological and functional development of interneurons, and whether retinal signaling is needed.

To examine these issues, we used the GAD67-GFP mouse to target developing dLGN interneurons during *in vitro* intracellular recordings. To assess whether retinal signaling plays a role in the development of their morphological and functional properties, we used a genetic form of retinal deafferentation by utilizing the math5 null (math5$^{-/-}$) mouse and crossing it onto the GAD67·GFP strain. These mutants lack the math5 gene that is required for retinal progenitors to differentiate into retinal ganglion cells (RGCs) (Brown et al., 1998). Consequently, math5$^{-/-}$ mice display a >95% loss of RGCs, fail to form an optic nerve, and thus leave dLGN devoid of retinal innervation (Brown et al., 2001; Wang et al., 2001; El-Danaf et al., 2015). This loss of function approach is advantageous to postnatal manipulations such as enucleation or optic nerve section. While "eyeless" phenotypes exist in the mouse, they are problematic because they involve a polygenic form of inheritance and additional mutations that likely have a deleterious impact on neuronal development (Cullen and Kaiserman-Abramof, 1976; Tucker et al., 2001; Verma and Fitzpatrick, 2007). Thus, we used math5$^{-/-}$ along with age·matched wildtypes GAD67·GFP to understand whether retinal signaling influences interneuron structure, function, and establishment of synaptic connectivity with dLGN relay neurons.

Materials and Methods

Animals

Experiments were conducted in mice of either sex ranging in age between P0-45. Two strains were used: GAD67-GFP (line G42; Jax stock no. 007677) established on a pigmented background (C57/B6 x CB6F1/J), and math5^{-/-} crossed onto GAD67·GFP. The math5^{-/-} strain was on a mixed C57/B6 and 129/SvEv background (Wang et al., 2001; El-Danaf et al., 2015). All procedures were approved by the University of Louisville Institutional Animal Care and Use Committee.

Acute in vitro thalamic slice preparation and whole-cell recording procedures

We used an acute thalamic slice preparation and conducted whole cell recordings on dLGN neurons using methods described in detail elsewhere (Govindaiah and Cox, 2006; Seabrook et al., 2013; El-Danaf et al., 2015). Briefly, mice were anesthetized with isoflurane, decapitated, and excised brains were placed in 4°C oxygenated (95% O_2/5% CO_2) slicing solution (in mM: 26 $NaHCO_3$, 234 sucrose, 10 $MgSO_4$, 11.0 glucose, 2.5 KCl, 1.25 NaH_2PO_4, 0.5 $CaCl_2$). A vibratome (Leica VT1200S) was used to make 270 μm-thick coronal sections containing dLGN. Slices were placed for at least 30 minutes in a 32°C oxygenated artificial cerebral spinal fluid (ACSF) (in mM: 126 NaCl, 26 $NaHCO_3$, 2.5 KCl, 1.25 NaH_2PO_4, 2 $MgCl_2$, 2 $CaCl_2$, and 10 glucose) and then maintained at room temperature. Throughout the recording, slices were continuously

perfused in an oxygenated solution of ACSF (2.5 ml/min, 95% O_2/5% CO_2) and maintained at 32°C.

Whole-cell recordings were obtained in both current-clamp and voltage-clamp mode using a chamber that was mounted on an upright microscope (Olympus BX51WI) equipped with DIC and florescence optics to visualize GFP-expressing interneurons. Recordings were made using a Multiclamp 700B amplifier (Molecular Devices), filtered at 3-10 kHz, and digitized (Digidata 1440A) at 10 kHz. Patch electrodes made of borosilicate glass were pulled using a vertical puller (Narshige PC-10) with a final tip resistance between 4-7 M$\Omega$$\Omega$.

For current clamp recordings, electrodes were filled with an internal solution containing (in mM): 117 K-gluconate, 13.0 KCl, 1 $MgCl_2$, 0.007 $CaCl_2$, 0.1 EGTA, 10 HEPES, 2 Na-ATP, and 0.4 Na-GTP). To examine the passive and active membrane properties of interneurons, we recorded the voltage responses evoked by square wave current pulses (-120 to +150 pA) of varying duration and intensity (600 and 1000 ms, 15 pA increments). Spike firing frequency (Hz) was based on maximal firing rate evoked by a large depolarizing current step. The degree of I_H-dependent inward rectification (V_{sag}) was determined by measuring the relative change between the maximal (V_{max}) and steady state (V_{ss},) voltage response: ($V_{max} - V_{ss}$ / V_{max}) * 100 (Leist et al., 2016).

To record inhibitory postsynaptic currents (IPSCs), we conducted voltage clamp recordings from dLGN relay neurons at 0 mV using a cesium-based internal solution containing (in mM): 117 Cs-gluconate, 11 CsCl, 1 $MgCl_2$, 1 $CaCl_2$, 0.1 EGTA, 10 HEPES, 2 Na_2-ATP, 0.4 Na_2-GTP. Concentrated stock

solution of (RS)-3,5-dihydroxyphenylglycine (DHPG) (Tocris catalog no. 0342) was prepared and stored as recommended. The agonist was diluted in ACSF to its final concentration (50 μM) prior to use, and applied via a short bolus into the input line of the recording chamber using a syringe pump (Govindaiah and Cox, 2006).

IPSCs were detected and analyzed with MiniAnalysis software (Synaptosoft, Leonia, NJ) using threshold (10 pA) and waveform detection protocols established by (Govindaiah and Cox, 2006). To quantify sIPSCs, the average frequency and amplitude were averaged from 120 second windows before mGluR5 agonist administration (pre), and after agonist administration (post).

For all recordings, biocytin (0.5%) was included in the internal solution to allow for intracellular filling and subsequent 3-D reconstruction using confocal microscopy. Following the completion of the recording session, slices were fixed overnight with 4% paraformaldehyde (PFA) in 0.1 M phosphate-buffered-saline (PBS) (pH = 7.2). To visualize biocytin-filled interneurons, slices were washed with PBS (3x, 10 min. each), and incubated overnight in PBS solution containing 0.1% Triton X-100 and 0.1% Alexa Fluor 647-conjugated streptavidin (Invitrogen, catalog no. S21374). The following day, slices were washed in PBS (3x, 10 min each), mounted with Prolong Gold with DAPI (Invitrogen, catalog no. P36931), and coverslipped for confocal imaging.

3-D reconstructions of biocytin-filled interneurons

Biocytin-filled interneurons were imaged using a multi-photon laser scanning confocal microscope (Olympus, model no. FV1200BX61). A HeNe laser (635nm) was used to excite far-red, biocytin fluorescence. Neurons were imaged using a 10x (0.3 NA) or 20x (0.75 NA) objective lens at a scanning resolution of 1600x1600 pixels. A sequential series of optical slices with an optimal step size through the Z-axis of 1.26 μm (20x/0.75 NA lens) created a 3-D, Z-stack dataset. Three-dimensional reconstructions and analysis were done using Imaris software (Bitplane, version 8.4.1). Soma area was measured by using the "Surface" function tool, and highlighting the soma in the X, Y, and Z planes. Branch reconstruction was generated in the Z-plane by using the "Filament tracer" function and verified by visual inspection. The total number of branches was determined by using the "Total Number of Terminal Points" tab in the Filament function. To evaluate the degree of arbor complexity, we labeled the filament-generated arbor tree using the "Statistics Coded Color" tab. This automated tool uses the soma as the starting point, and traces the arbor tree according to n^{th} order branch. The "Statistics" tab was used to calculate the average and maximal branch order for each interneuron. To measure the volume of the arbor field, we started with the filament reconstruction, and used the "Convex Hull XTension" function in the Tools tab. This feature creates a new surface object superimposed on the filament. The convex polyhedron envelops all distal points (i.e. distal processes) of the selected filament and is used to calculate volume.

Experimental design and statistical analysis

All statistical tests were performed using either SigmaPlot 11.0 (Systat Software,

San Jose, CA) or Prism 7.0 (Graphpad Software, La Jolla, CA). To test for

normality, we utilized the Shapiro-Wilk Normality and Equal Variance Test. A

Two-way ANOVA was used to examine age-related differences within a group

(WT or math5$^{-/-}$) and between groups across the various morphological features

(e.g., soma area, arbor complexity, arbor field volume) and membrane properties

(V_{sag}, firing frequency). The *post-hoc* Holm-Sidak method allowed for pairwise

multiple comparisons both within group and across postnatal weeks. For

pharmacology experiments, we conducted a two-way ANOVA repeated

measures to assess pre- vs post-drug differences in IPSC frequency and

amplitude. The *post-hoc* Holm-Sidak method was applied to make multiple

comparisons between groups. To compare percent changes in mGluR$_5$ agonist-

mediated responses ((Post–Pre / Pre) * 100) we used the non-parametric Mann-

Whitney rank sum test to determine whether median values of frequency and

amplitude were different between WT and math5$^{-/-}$. For all statistical tests, p

values <0.05 were considered significant.

Results

Morphology of developing interneurons in WT and math5$^{-/-}$ mice

Figure 1 shows examples of coronal sections through the dLGN of P5 (A) and

P21 (B) GAD67·GFP (WT) and GAD67 x math5$^{-/-}$ (math5$^{-/-}$) mice. In both strains,

we observed GFP labeling in dLGN interneurons even at early postnatal ages. In

WT, interneurons are evenly distributed throughout the nucleus (Seabrook et al.,

2013; Golding et al. 2014). However, in math5$^{-/-}$, interneurons failed to migrate

properly and clustered in the upper sector of the dLGN. This observation is

consistent with previous reports showing that early postnatal elimination of retinal

signaling disrupts the migratory path and spacing of dLGN interneurons (Golding

et al., 2014). Nonetheless, in both strains we were able to readily identify and

target interneurons for recording and biocytin filling.

   We generated 3-D reconstructions for a total of 130 biocytin-filled

interneurons (WT, n = 64; math5$^{-/-}$, n = 66) across the first four weeks of

postnatal life. Figure 2 provides representative examples of interneuron

reconstructions from WT and age-matched math5$^{-/-}$ mice arranged by postnatal

week. At early ages and in both groups, interneurons had Type II morphology,

displaying expansive and complex arbors that arise from opposite poles of

fusiform-shaped soma (Guillery, 1966). Arbors are comprised of both dendrites

and axons. Not all interneurons have conventional axons, and there is no clear

way to distinguish them from dendrites (Lieberman, 1973; Wilson, 1986;

Sherman, 2004). Additionally, bead-like protrusions on distal processes (Fig. 2,

inset) were especially apparent in WT after the second postnatal week. It is

presumed these grape-like appendages represent pre-synaptic dendritic terminal sites (F2 profiles) that form part of a triadic arrangement with a retinal terminal and relay cell dendrite (Szentagothai, 1963; Guillery, 1966; Hamos et al., 1985; Sherman, 2004). Despite the similarities in overall morphology between WT and math5^{-/-} interneurons, the absence of retinal signaling had a dystrophic effect on their growth and these defects are summarized in Fig. 3.

WT interneurons experienced significant growth in soma size between weeks 1 and 2 (Fig. 3A black, $F_{(3, 120)}$ = 3.722; p = 0.013), displaying ~2-fold change in area (p = 0.026). After the second postnatal week, soma size stabilized. By contrast, math5^{-/-} somata did not undergo an age-related change, remaining constant between weeks 1-4 (Fig. 3A red, $F_{(3, 120)}$ = 3.722; p = 0.884). Comparisons with WT revealed math5^{-/-} interneuron somata were significantly smaller between weeks 2-4 ($F_{(1, 120)}$ = 36.54; week 2 p < 0.0001, week 3 p = 0.0015, week 4 p = 0.0066).

To assess the development of arbor architecture, we examined the total number of processes, branch order, and size of the arbor field. (Fig. 3B-D). When considering these features, all branching elements (presumed axons and dendrites) were included in the analyses. WT interneurons undergo a number of age-related changes in arbor architecture (Fig. 3B-D, black). For example, there was a significant increase in the total number of processes (Fig. 3B, $F_{(3,122)}$ = 18.65, p < 0.0001). Between weeks 1-2 the total number of processes increased ~3-fold (p < 0.0001). However, this increase was transient, and following the second postnatal week, the number of processes showed a significant decrease

by nearly 40% ($p < 0.001$). Despite this pruning, the number of arbors during week 4 was still 1.6-fold greater than week 1 ($p = 0.003$). These changes were accompanied by a significant increase in branch order (Fig. 3C, $F_{(1, 120)} = 19.09$, $p < 0.001$). For instance, between weeks 1-2, branch order nearly doubled from 4th order to 9th order, with some cells exhibiting as high as 12th order branching ($p < 0.001$). WT branch order also decreased during weeks 2-3, from 9th to 6th order ($p < 0.001$), and at week 4 remained higher than week 1 ($p = 0.029$). Finally, dLGN interneurons experienced a significant change in arbor field size (Fig. 3D, $F_{(3, 137)} = 3.307$; $p = 0.012$). Between weeks 1-2, arbor volume doubled ($p = 0.022$) and then stabilized ($p = 0.998$). Overall, these data suggest that interneuron arbors undergo an exuberant branching phase between weeks 1-2, then prune back during week 3 when their architecture stabilizes to resemble their adult-like form.

Unlike WT, math5$^{-/-}$ interneurons failed to show many of these changes (Fig. 3B-C, red). The number of processes and branch complexity remained stable across age (total processes, $F_{(3, 122)} = 18.65$, $p = 0.9666$; branch complexity, $F_{(3, 120)} = 19.09$, $p = 0.580$), and after week 1, these features were significantly reduced compared to WT (total processes, $F_{(1, 122)} = 104.87$; $p < 0.001$; branch complexity, $F_{(1, 120)} = 83.17$, $p < 0.001$). Interestingly, math5$^{-/-}$ interneurons undergo a 2.5-fold retraction in arbor field size between weeks 3-4 ($p = 0.022$) and were significantly smaller than WT (Fig. 3D, $F_{(1, 137)} = 16.348$; week 2 $p = 0.006$, week 4 $p = 0.023$). Thus, these results demonstrate that

math5^{-/-} interneurons fail to remodel and maintain a simple, sparse morphology throughout development.

Intrinsic membrane properties of WT and math5^{-/-} interneurons

To assess the development of intrinsic membrane properties, we evaluated resting membrane potential (RMP), input resistance, the hyperpolarization-activated mixed cation conductance I_H, and the frequency of spike firing frequency. Figure 4 provides representative examples of the voltage responses of interneurons evoked by square wave hyperpolarizing (Fig. 4, top) and depolarizing (Fig. 4, bottom) current pulses for WT (P3-30, n = 68 cells) and math5^{-/-} (P4-30, n = 75 cells). Overall, neurons exhibited a relatively high membrane input resistance, which led to a strong voltage response to current injection. A prominent feature of interneurons is the presence of an inward rectification (i.e. depolarizing sag, V_{sag}) that occurs during membrane hyperpolarization, a response attributed to the activation of the mixed cation conductance (I_H) (Williams et al., 1996; Seabrook et al., 2013; Leist et al., 2016). Membrane depolarization also gave rise to a train of action potentials that showed little to no frequency accommodation. These properties were apparent in both WT and math5^{-/-} interneurons, and began to emerge between weeks 1-2.

Figure 5A-B summarizes the age-related changes in RMP and input resistance of dLGN interneurons. In WT, RMP and input resistance remained relatively stable with age, averaging -56 mV and 450-460 M$\Omega\Omega$, respectively (Fig. 5A-B, black; RMP, $F_{(1, 137)}$ = 1.132, p = 0.854; input resistance, $F_{(1, 130)}$ = 2.178, p = 0.702). A similar pattern was apparent in math5^{-/-} interneurons (Fig. 5A-B,

red; RMP, -50 mV and input resistance, 660-670 M$\Omega\Omega$) (RMP, $F_{(1, 137)}$ = 1.132, p = 0.259; input resistance, $F_{(1, 130)}$ = 2.178, p = 0.472). However, these values were different from WT. In math5^{-/-}, RMPs were more depolarized between weeks 1-2 (Fig. 5A, $F_{(1,137)}$ = 18.01; week 1 p = 0.003, week 2 p = 0.035), and overall input resistance was higher at all ages (Fig. 5B, $F_{(1,130)}$ = 17.65; all p values < 0.038) a result likely due to the their smaller soma size (Fig. 3A). We also examined I_H by measuring the amplitude of the depolarizing sag as a percent change from steady state (V_{sag}). In WT, interneurons exhibited a 1.5-fold change between weeks 1-2 (Fig. 5C, $F_{(2, 127)}$ = 5.648; p = 0.044), and stabilized thereafter (p = 0.589). Maximal spike firing to strong depolarizing current pulses (-120-150 pA) showed a 2-fold increase between weeks 1-2 (Fig. 5D, $F_{(2, 138)}$ = 8.254; p = 0.037), and then stabilized (p = 0.607).

By contrast, in math5^{-/-}, I_H remained relatively stable with age (Fig. 5C, $F_{(2, 138)}$ = 2.47, p = 0.351), along with a 6-fold increase in spike firing between weeks 1-2 ($F_{(2, 138)}$ = 8.254, p = 0.005). Compared to WT, math5^{-/-} showed significantly lower values for V_{sag} and maximal spike firing (Fig. 5C-D, I_H, $F_{(1, 127)}$ = 14.537, p < 0.001; firing frequency $F_{(1, 138)}$ = 14.764, p < 0.001), due largely to the differences seen during week 2 (I_H, p = 0.002; firing frequency, p = 0.015). Thus, these results reveal that math5^{-/-} interneurons remain functionally immature.

Synaptic connectivity between dLGN interneurons and relay neurons

To study the synaptic connectivity between interneurons and relay cells, we measured the frequency and amplitude of inhibitory postsynaptic currents

(IPSCs) in relay neurons that were pharmacologically evoked by the activation of F2 terminals. These processes express the Group I metabotropic glutamate receptor 1,5 ($mGluR_{1,5}$), and the bath application of the agonist (RS)-3,5-dihydroxyphenylglycine (DHPG) evokes F2-mediated $GABA_A$ receptor mediated inhibition onto relay neurons (Cox et al., 1998; Cox and Sherman, 2000; Govindaiah and Cox, 2006). Figure 6 shows examples of biocytin-filled relay cells in WT (A) and math5^{-/-} (B) along with their corresponding IPSC activity (5 min) recorded before, during, and after DHPG application. As summarized in Figure 7A-B, during pre-drug conditions there were no differences in IPSC activity between WT and math5^{-/-} (frequency, $F_{(1,54)}$ = 35.03; p = 0.950; amplitude, $F_{(1,54)}$ = 0.623, p = 0.106). However, WT neurons (n = 23 cells, n = 59, 061 IPSCs) showed a significant increase in IPSC frequency and amplitude following DHPG treatment that persisted for several seconds (120-420 s, Fig. 7A, frequency $F_{(1,54)}$ = 35.03, p < 0.0001; Fig. 7B amplitude, $F_{(1,54)}$ = 0.623, p = 0.0004). IPSC frequency more than doubled with amplitude showing a 1.3- fold change after agonist application. In math5^{-/-}, relay cells (n = 33 cells, n = 50,676 IPSCs) showed a modest increase in IPSC frequency (Fig. 7A, $F_{(1,54)}$ = 35.03, p = 0.018) and no change in amplitude (Fig. 7B, $F_{(1,54)}$ = 0.623, p = 0.995) following DHPG application. Moreover, post-drug math5^{-/-} IPSC frequency as well as amplitude were significantly lower than WT (p < 0.0001).

In order to demonstrate the differences in magnitude of the DHPG-evoked increase in IPSCs between the two groups, for each neuron we calculated the percent change in IPSC frequency (Fig. 7A, right) and amplitude (Fig. 7B, right)

for each neuron. Overall, WT relay neurons displayed far greater changes (95 %

confidence interval of the mean; frequency 120-260%, amplitude 10-50%),

showing significantly higher values than math5$^{-/-}$ (95% confidence interval of the

mean; frequency 20-40%; amplitude -5-10%; Mann-Whitney Rank Sum Test, p <

0.0001). Taken together, these data suggest that the absence of retinal signaling

disrupts the synaptic connectivity between intrinsic interneurons and relay
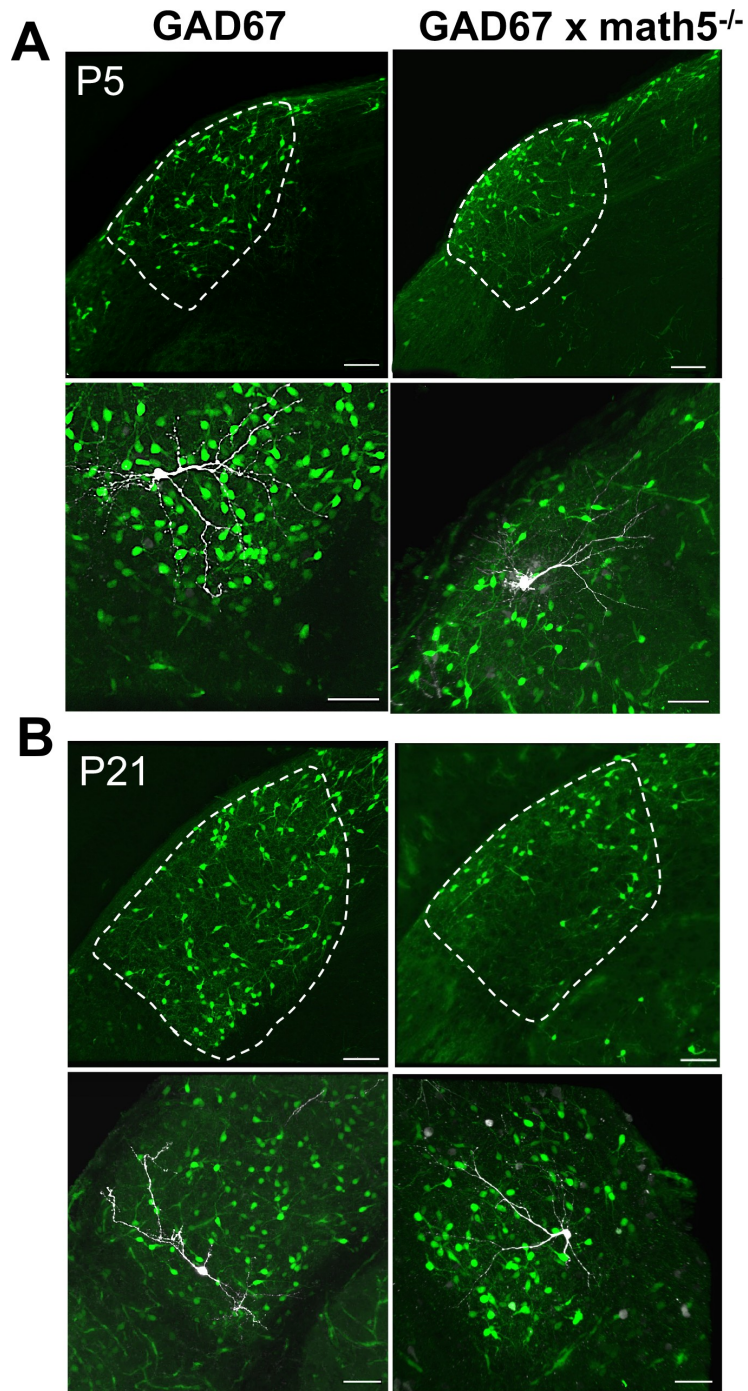
neurons.

Figure 13: Green fluorescent protein (GFP) expressing interneurons in dorsal lateral geniculate nucleus (dLGN) of WT and math5$^{-/-}$ mice.

A: Coronal sections of dLGN from a P5 GAD67 WT mouse (left) and math5$^{-/-}$ (right) crossed onto the GAD67 strain. *Top*: In WT, interneurons are evenly

distributed throughout dLGN, however in math5$^{-/-}$, migration is disrupted and they cluster in the dorsolateral region (Golding et al., 2014) Scale bar = 70 um. *Bottom*: Examples of GFP-expressing interneurons that were filled with biocytin during *in-vitro* intracellular recordings and used for 3-D reconstructions. Scale bar = 40 um. **B:** Coronal sections of dLGN from P21 WT and math5$^{-/-}$ mice. *Top*: Distribution of GFP-expressing interneurons in dLGN. *Bottom*: Examples of biocytin-filled interneurons.
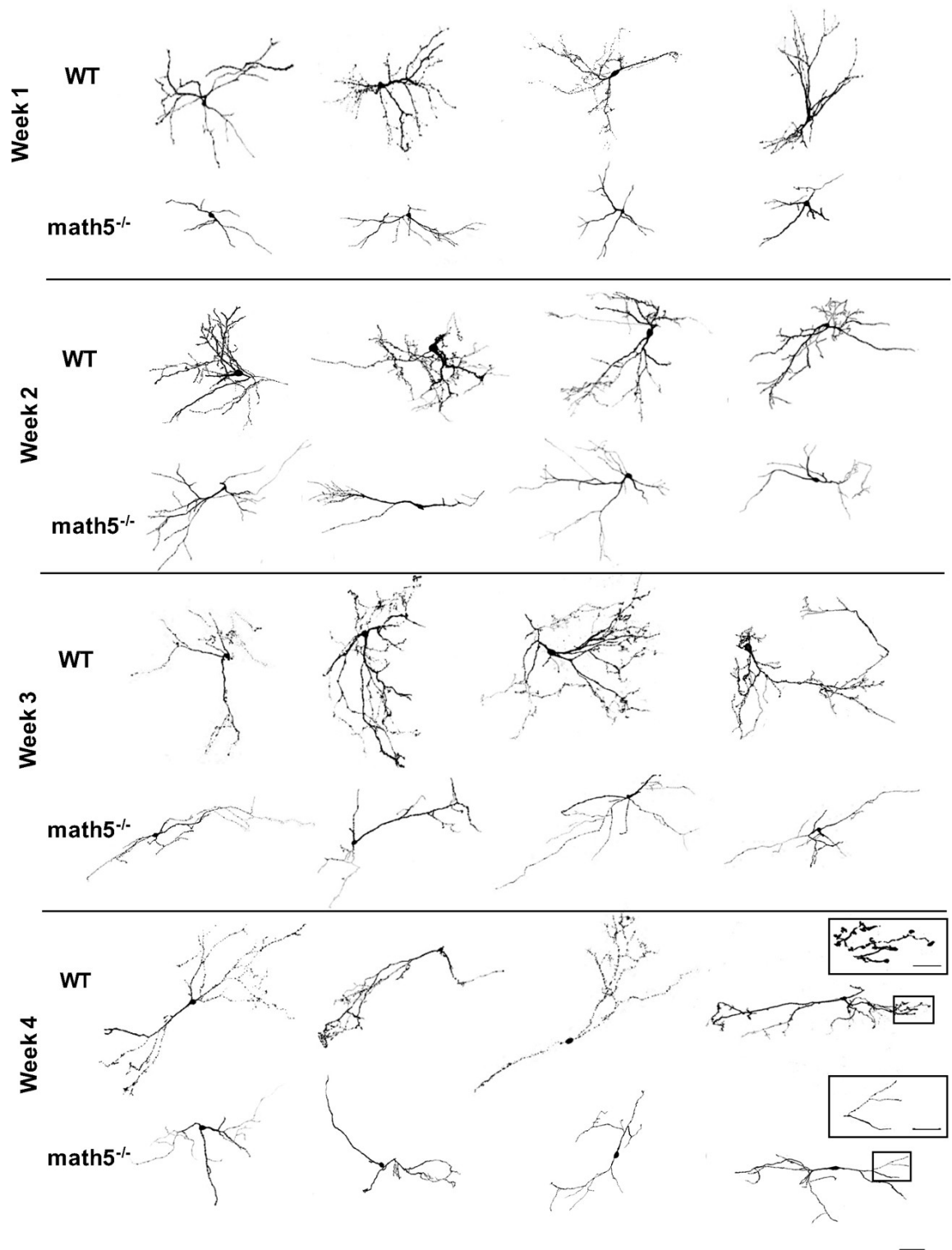
Figure 14: Biocytin filled interneurons in dLGN of WT and math5$^{-/-}$ mice.

Examples of interneurons arranged by postnatal week (1-4) for WT (top row) and

math5$^{-/-}$ (Bottom row). Reconstructions are based on Z-stacked confocal images of biocytin-filled interneurons. Scale bar = 50 μm; inset scale bars = 5 um.
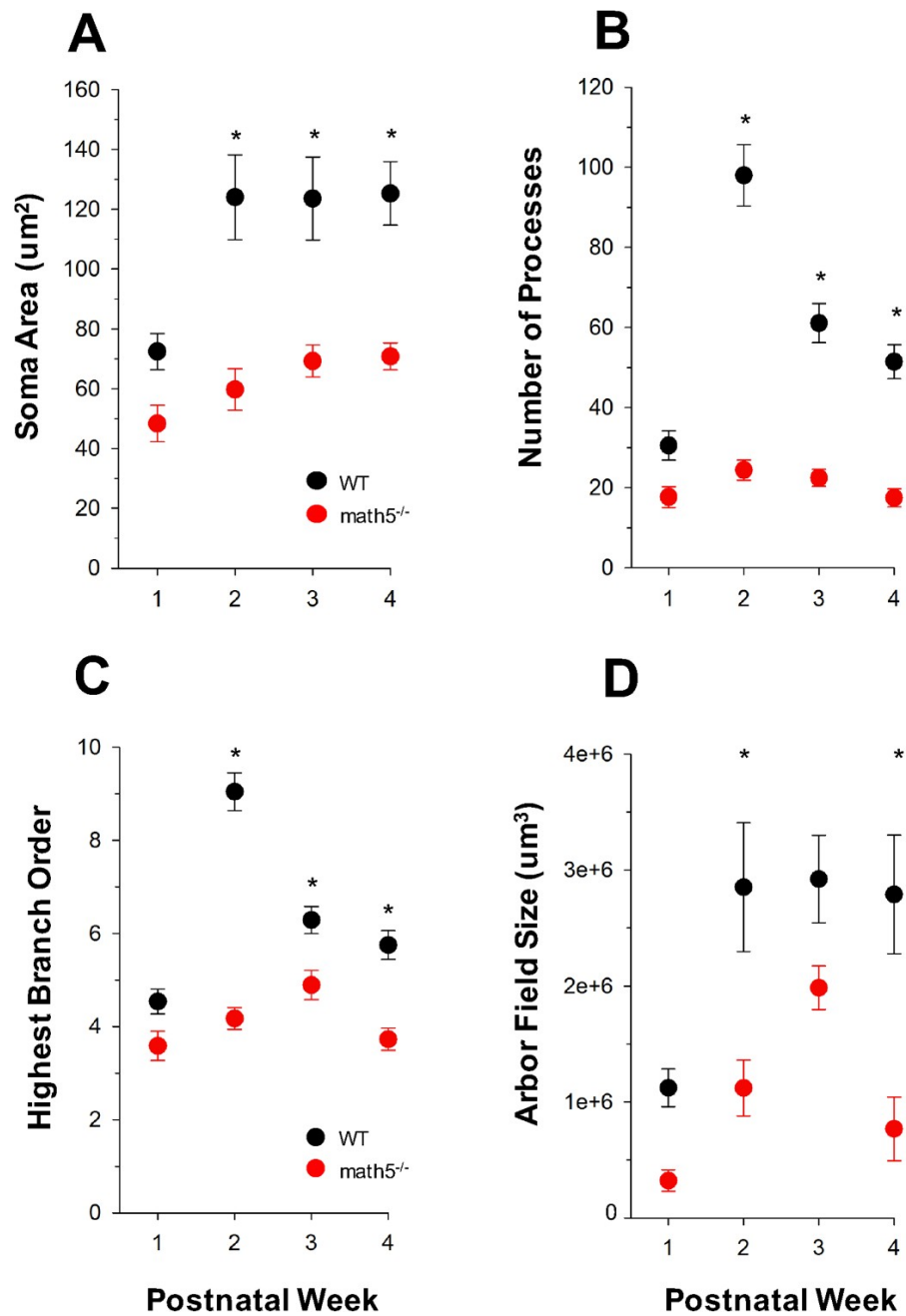
Figure 15: Morphological development of dLGN interneurons in WT and math5$^{-/-}$ mice.

Summary plots depicting age-related changes in soma area (**A**), number of

processes (**B**), branch complexity (**C**), and arbor field size (**D**) of interneurons in

WT (black) and math5$^{-/-}$ (red). Each point represents mean values +/- SEM plotted by postnatal week. **A:** Between weeks 1-2, WT soma area increased ~2-fold (*, p = 0.026). Math5$^{-/-}$ soma areas are reduced compared to WT between weeks 2-4 (*, week 2 p < 0.001, week 3 p = 0.0015, week 4 p = 0.0066). **B:** WT interneurons show increased number of arbor processes between weeks 1-2 (*, p < 0.0001), followed by a reduction in weeks 3-4. Math5$^{-/-}$ interneurons show no age-related changes, and are reduced compared to WT during weeks 2-4 (*, weeks 2-4 p < 0.001). **C:** WT interneurons display increased higher-order branching between weeks 1-3, (*, week 2 p < 0.0001, week 3 p = 0.029). Math5$^{-/-}$ interneurons display decreased complexity compared to WT between weeks 2-4 (*, week 2 p < 0.001, week 3 p = 0.014, week 4 p = 0.002). **D:** Math5$^{-/-}$ interneurons displayed smaller arbor field sizes during weeks 2 and 4 (*, week 2 p = 0.006, week 4 p = 0.023), and experience field retraction during week 4 (*, p = 0.022).

For all analyses, WT: week 1, n = 3 mice, n = 10 cells; week 2, n = 7 mice, n = 24 cells; week 3, n = 4 mice, n = 17 cells; week 4, n = 3 mice, n = 14 cells. Math5$^{-/-}$: week 1, n = 4 mice, n = 12 cells; week 2, n = 5 mice, n = 24 cells; week 3, n = 5 mice, n = 18 cells, week 4, n = 3 mice, n = 12 cells.
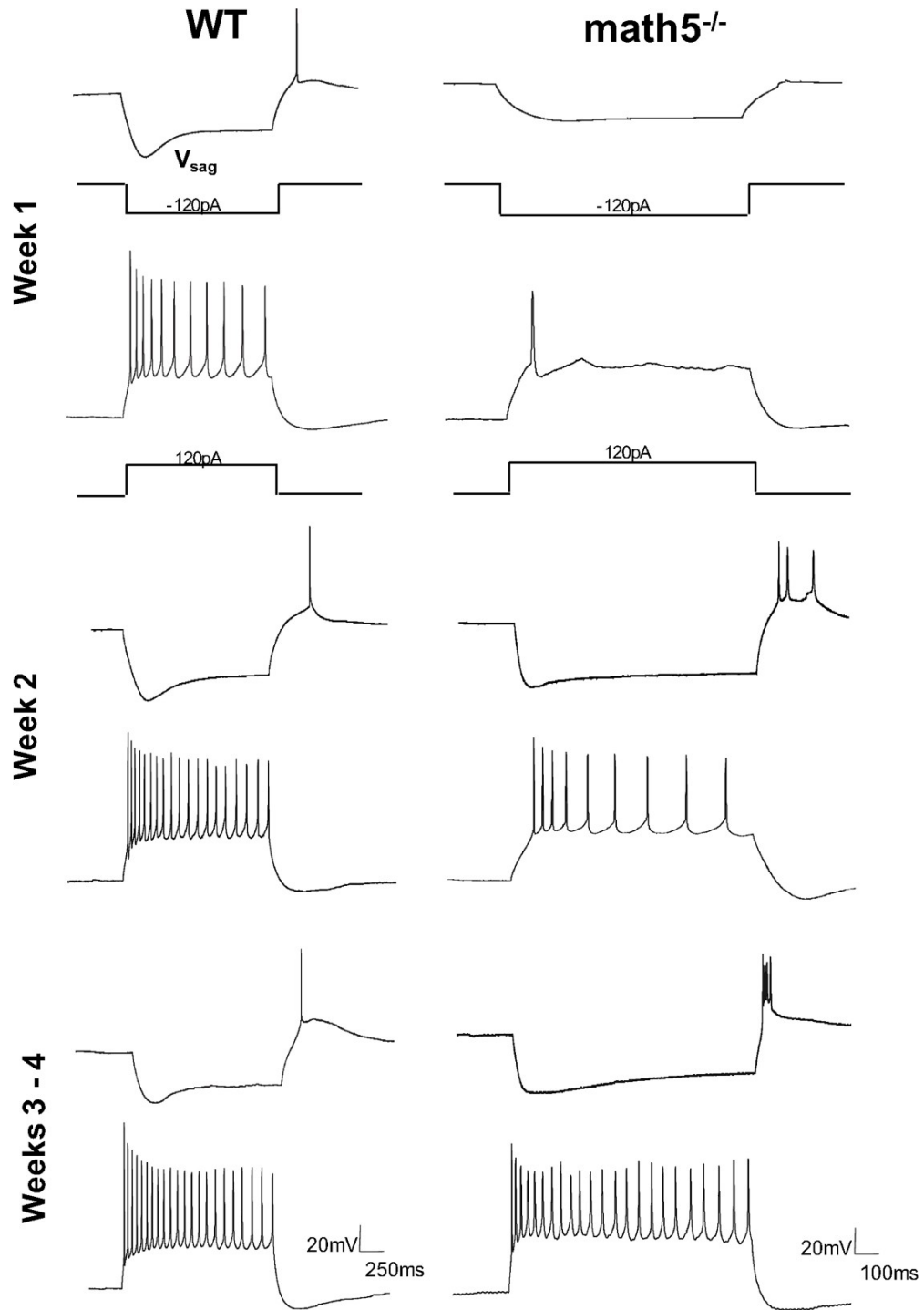
Figure 16: Intrinsic membrane properties WT and math5$^{-/-}$ interneurons.

Examples of voltage traces showing responses to hyperpolarizing (-120 pA) and

depolarizing (150 pA) current step pulses from interneurons at different postnatal weeks (1-4) for WT (left) and math5$^{-/-}$ (right); WT RMP: -55-60 mV; math5$^{-/-}$ RMP: -45-50 mV. For WT, interneurons exhibit a strong inward rectification (V_{sag}) to hyperpolarizing pulses following the termination of the current pulse. Membrane depolarization evokes a train of action potentials. In math5$^{-/-}$, interneuron responses remain relatively immature.
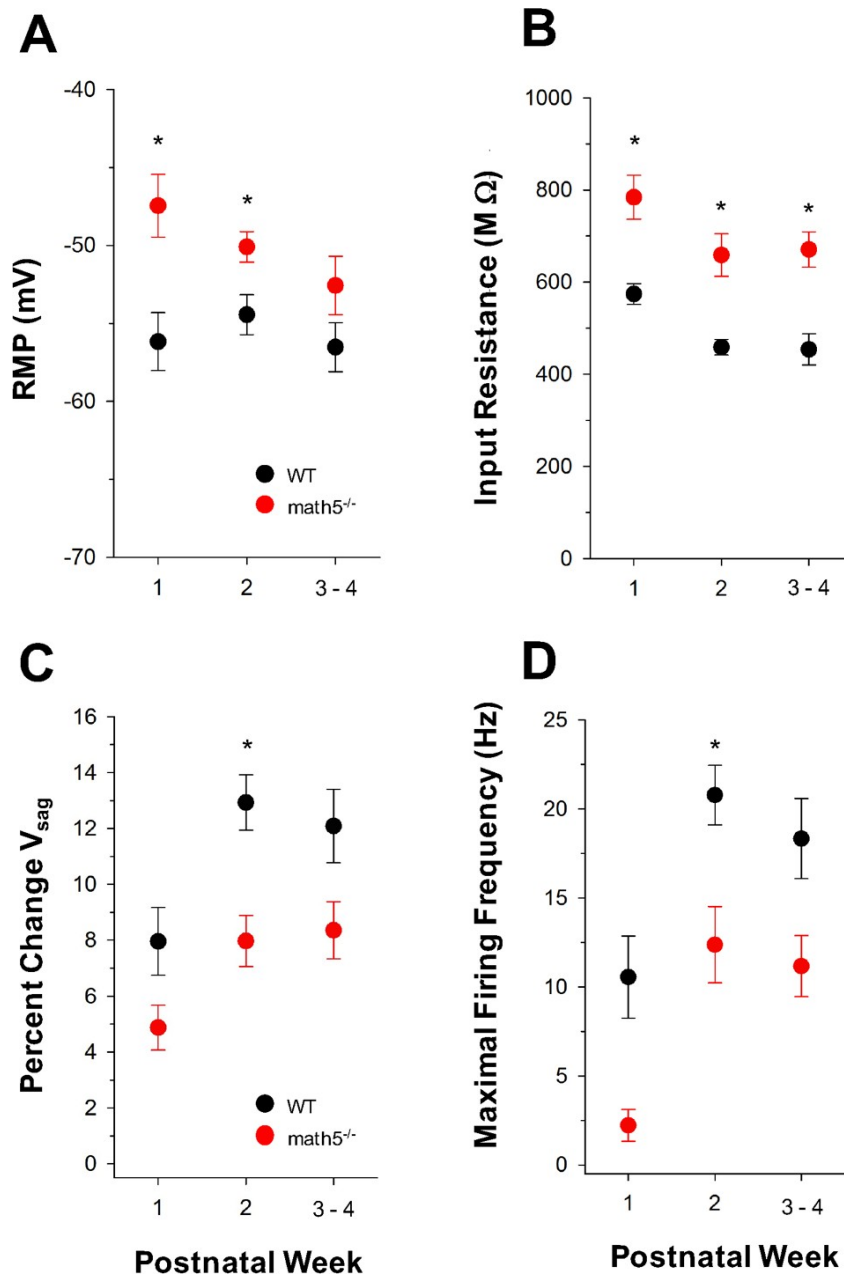
Figure 17: Passive and active membrane properties of WT and math5$^{-/-}$ interneurons. Scatter plots displaying age-related changes in resting membrane potential **(A)**, input resistance **(B),** I$_H$ amplitude **(C)**, and firing frequency **(D)** of interneurons in WT (black) and math5$^{-/-}$ (red). Each point represents mean values

+/- SEM arranged by postnatal week. **A:** Math5$^{-/-}$ interneurons exhibit more depolarized RMPs at weeks 1 and 2 (*, week 1 p = 0.003, week 2 p = 0.035). **B:** At all ages, math5$^{-/-}$ interneurons have a higher input resistance (*, week 1 p = 0.038, week 2 p = 0.013, weeks 3-4 p = 0.027). **C:** WT interneurons show increases in I$_H$ conductance between weeks 1-2 (*, p = 0.029), whereas math5$^{-/-}$ interneurons show no change and are decreased compared to WT (*, p = 0.002). **D:** In WT, interneurons experience a 2-fold increase in frequency between weeks 1-2 (*, p = 0.005). Between weeks 1-2, math5$^{-/-}$ interneurons also show increases in frequency (*, p = 0.0006), but remain decreased compared to WT (*, p = 0.015). Numbers of cells same as Figure 3.
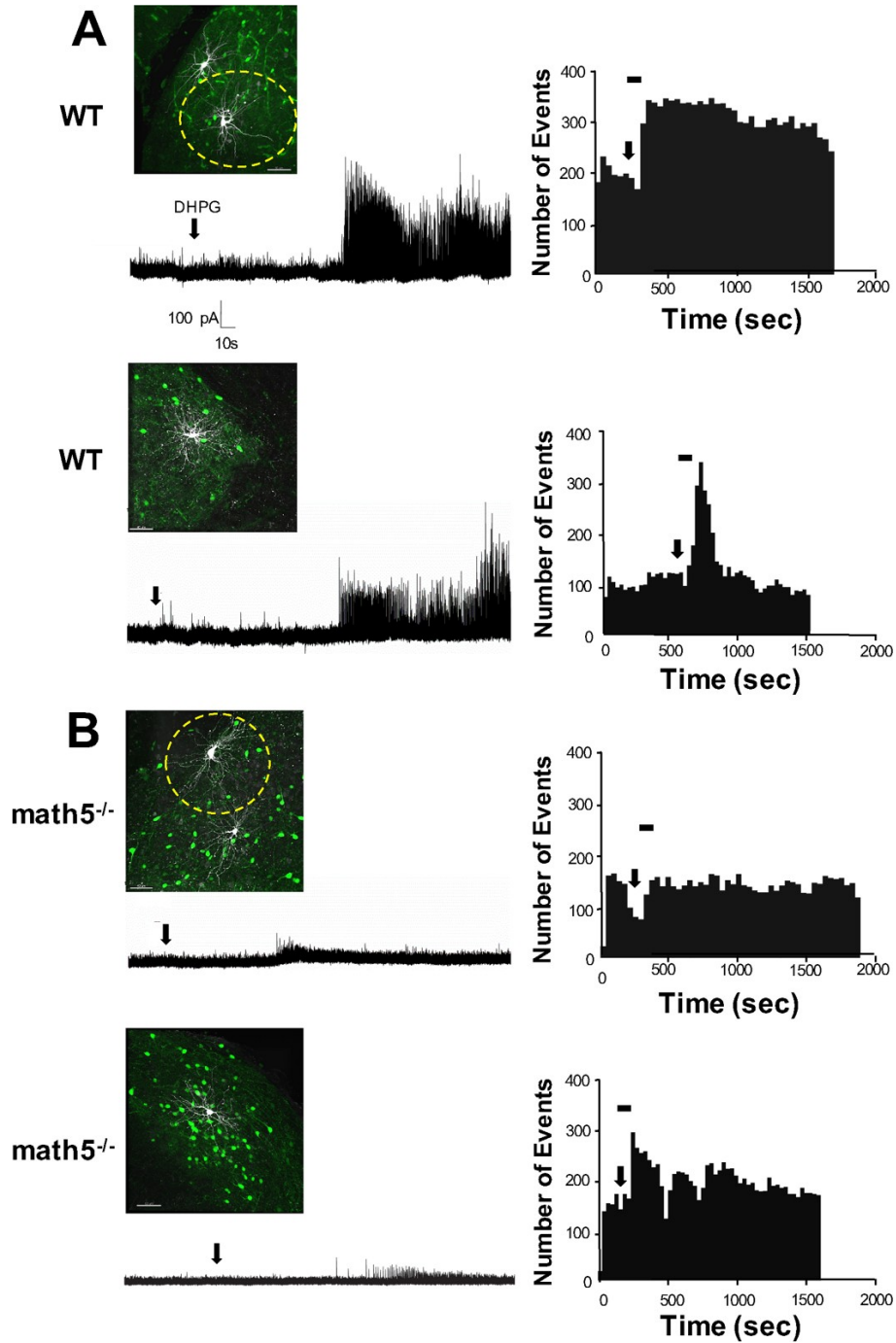
Figure 18: Pattern of spontaneous inhibitory activity in relay neurons in WT and math 5$^{-/-}$ mice. Examples of WT (A) and math5$^{-/-}$ (B) dLGN relay neurons (Scale bar = 40 um) and their corresponding spontaneous inhibitory postsynaptic

current (IPSC) responses before and after bath application of mGluR$_5$ DHPG (50 μM). Arrows depict the time of drug delivery. Adjacent to the responses are the corresponding frequency histograms that plot the number of inhibitory events as a function of time. Horizontal bars reflect the adjacent current responses. Bin width is 30 sec. Activation of metabotropic glutamate receptor 1,5 (mGluR$_{1,5}$) leads to a sustained increase in IPSC activity in WT and little or no change in math5$^{-/-}$.
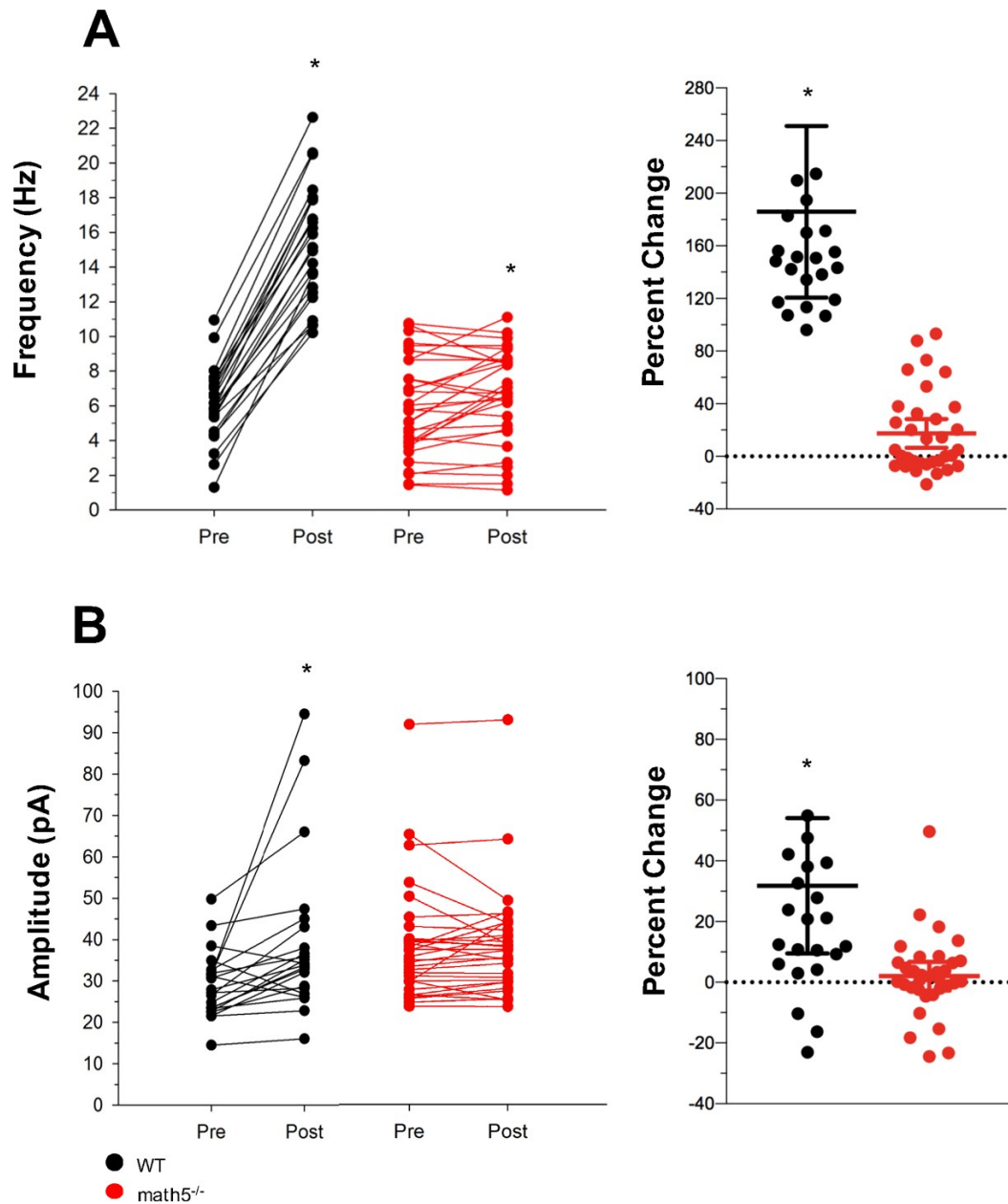
Figure 19: IPSC frequency and amplitude response before and after mGluR5 activation in WT and math5$^{-/-}$ relay neurons.

A: *Left*: Scatter plot showing DHPG-induced changes in IPSC frequency for WT (black) and math5$^{-/-}$ (red). Solid lines and dots depict pre- and post-DHPG

measurements from individual relay neurons (WT, n = 23; math5$^{-/-}$, n = 33). WT

cells display higher post-DHPG frequencies compared to math5$^{-/-}$ (*, p < 0.0001).

Right: Scatterplot illustrating the percent change frequency for each relay cell.

Horizontal bars are means and 95% confidence intervals. **B:** *Left*: Scatter plots

showing the DHPG-induced changes in IPSC amplitude. Only WT relay neurons

showed an increase (*, p = 0.033). *Right:* Summary plot of drug effect expressed

as percent change. WT cells showed increased amplitude percent change

compared to math5$^{-/-}$ (*, p = 0.0002).
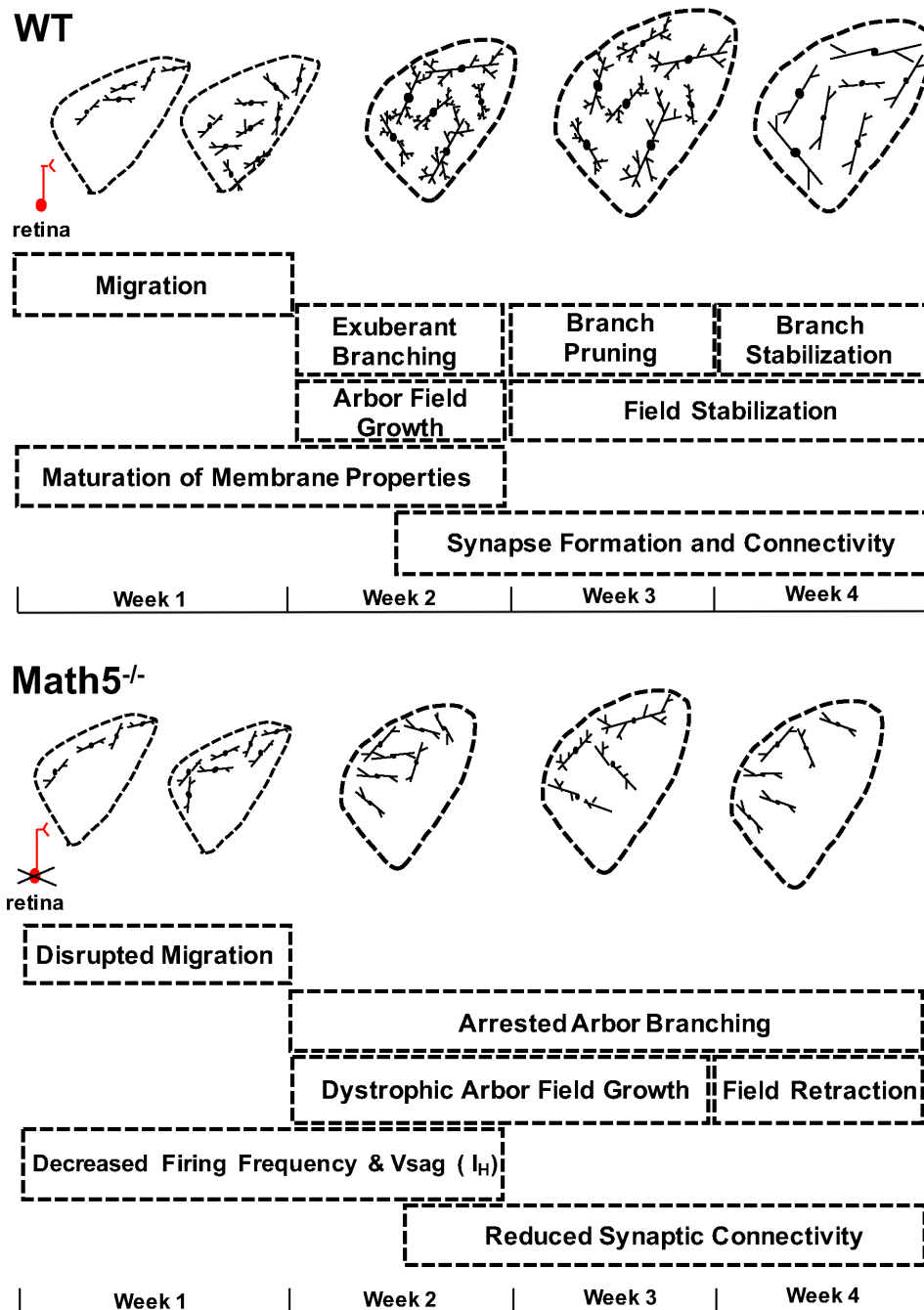
Figure 20: Development of interneurons in WT and math5$^{-/-}$ mice. Schematic summarizing the timeline of WT (top) and math5$^{-/-}$ (bottom) interneuron development. Boxes indicate various WT milestones: migration (Golding et al., 2014), arbor remodeling (i.e., exuberant branching, pruning, and stabilization),

arbor field growth and stabilization, maturation of membrane properties, and synapse formation and connectivity. For math5$^{-/-}$, the absence of retinal signaling results in disrupted migration, arrested arbor branching, dystrophic arbor field growth, decreased firing frequency/V_{sag}, and reduced patterns of synaptic connectivity.
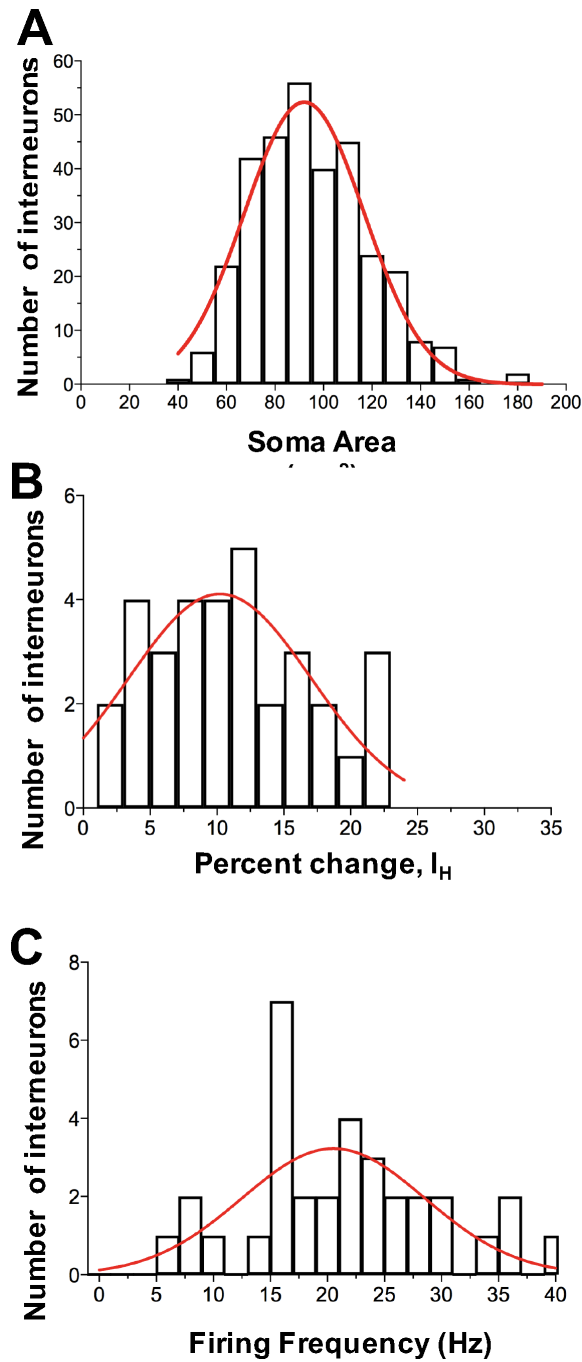
Figure 21: Frequency distribution of soma size, V_{sag}, and spike firing of WT interneurons. **A:** Frequency distribution of soma areas of GFP-expressing interneurons measured from coronal slices of dLGN at ages when soma size has stabilized (P14+, n = 3 animals, 3 sections per animal). Red solid line represents

single Gaussian fit generated from nonlinear regression analysis to fit all data points (μ = 92.08, σ = 24.71). **B:** Examination of data from Fig. 5 to determine if there is a bimodal distribution of percent changes in I_H. Nonlinear regression analysis revealed single Gaussian curve best fits the data (μ = 10.22, σ = 6.831). **C:** Same set of cells in (B) to examine distribution in firing frequency, which also followed a single Gaussian function (μ = 12.63, σ = 17.56).

Discussion

      A number of studies in mouse describe how and when interneurons migrate to dLGN and make feedforward inhibitory connections with relay neurons (Bickford et al., 2010; Seabrook et al., 2013; Golding et al., 2014; Jager et al., 2016). Here we provide additional details about their morphological growth and the emergence of adult-like membrane properties to present a comprehensive timeline of interneuron development (Fig. 8, top). In addition, our experiments in math5$^{-/-}$ mutants reveal that many of these features require retinal signaling (Fig. 8, bottom).

      At perinatal ages, interneurons begin to migrate to dLGN, and become evenly dispersed throughout the nucleus by the end of the first postnatal week (Fig. 8, *migration)* (Golding et al., 2014; Jager et al., 2016). Once migration is complete, arbor elaboration and remodeling begins. By the second postnatal week, the number of processes, arbor complexity, and arbor field size exhibit substantial increases (Fig. 8, *exuberant branching and arbor field growth)*. During this time, intrinsic membrane properties are maturing, as I_H (V_{sag}) and firing frequency reach peak values (Fig. 8, *maturation of membrane properties*). Interestingly, this phase of exuberant growth is followed by a brief period of arbor pruning in week 3, where the number of processes and complexity decrease (Fig 8, *branch pruning*). By week 4 the arbor architecture stabilizes and interneurons assume a stereotypic, Type II morphology (Fig 8, *branch and field stabilization*). Moreover, during the active period of arbor remodeling (*exuberant branching and*

91

pruning) feedforward inhibitory synapses emerge (Fig. 8, *synapse formation and connectivity*) (Bickford et al., 2010).

According to a recent report, dLGN interneurons are comprised of two classes based on soma diameter, with smaller ones having a higher density of I_H channels and higher rates of firing compared to larger ones (Leist et al., 2016). However, in our study we failed to find such distinctions. For example, in WT soma area (μm^2) measurements of interneurons were normally distributed and best fit by a single Gaussian function. Similar relationships were found for the amplitude of I_H V_{sag} and spike firing frequency (Fig. 8-1, Extended Data). The reasons for such discrepancy remain unclear but may be related to differences in the measurement of soma size, the primary distinguishing factor (e.g. 3-D area vs. 2-D diameter).

Our results in math5 mutants reveal that the absence of retinal innervation disrupts many aspects of interneuron development (Fig. 8, bottom). Consistent with other reports, the elimination of retinal signaling leads to abnormal clustering of interneurons, and a failure to distribute evenly throughout dLGN (Fig. 8, *disrupted migration*) (Golding et al., 2014). Additionally, based on our 3-D reconstructions, math5^{-/-} interneurons do not undergo arbor remodeling during postnatal development. Instead, they maintain simple, sparse arbors at all ages (Fig. 8, *arrested arbor branching*). The size of their arbor field is also restricted (Fig. 8, *dystrophic arbor field growth*), and during the fourth postnatal week fields actually retract (Fig. 8, *field retraction*). Functionally, the intrinsic membrane properties of math5^{-/-} interneurons fail to mature, and exhibit decreased spike

firing rates and weaker V_{sag} (Fig. 8, *decreased firing frequency and I_H*).

Furthermore, the elimination of retinal signaling also leads to a disruption in

feedforward inhibition. Recordings in math5^{-/-} relay cells show little change in

IPSC frequency after pharmacological activation of F2 terminals. By contrast, WT

relay neurons exhibit a 2 to 4-fold increase in IPSC frequency (Cox and

Sherman, 2000; Govindaiah and Cox, 2006). These findings suggest that math5^{-/-}

contain fewer and/or weaker inhibitory synapses (Fig. 8, *reduced synaptic

connectivity*). These results are consistent with previous studies that employ

early postnatal elimination of retinal signaling (Golding et al., 2014). However, the

utility of a genetic form of deafferentation (i.e., math5^{-/-}) rules out the possibility

that these disruptions were brought about by trauma or degeneration. Instead

they are likely a consequence of stunted arbor growth or the abnormal clustering

of interneurons that occurs after the removal of retinal innervation. Interestingly,

WT and math5^{-/-} relay neurons display similar baseline IPSC activity, suggesting

inhibitory input from extrinsic sources (e.g., pretectum, thalamic reticular nucleus)

are intact and may act to compensate for the loss of intrinsic inhibition. Such

compensatory activity may reflect a form of homeostatic plasticity designed to

maintain proper E/I balance (Turrigiano and Nelson, 2004; Maffei et al., 2006).

The current study elucidates the importance of retinal signaling, and its

role in supporting the morphological development and emergence of feedforward

inhibitory connections in dLGN. These findings are consistent with previous

studies from our lab demonstrating that retinal input provides vital trophic support

for the morphological development of dLGN relay cells (El-Danaf et al., 2015).

Furthermore, our results imply that retinal signaling has a greater impact on interneurons than on relay cells. Although math5$^{-/-}$ relay neurons experience dystrophic dendritic growth, they retain relatively complex dendritic architecture, cell-class identity, and the full complement of voltage gated membrane properties (El-Danaf et al., 2015). By contrast, dLGN interneurons in math5$^{-/-}$ fail to remodel, and instead remain morphologically and functionally immature.

While it is evident that retinal axons provide some form of trophic support for dLGN interneurons, the underlying molecular mechanism remains unknown. One prospect is brain-derived neurotrophic factor (BDNF). This growth factor is synthesized in RGCs and released by retinal axons, where it binds to receptor tyrosine kinase (trkB) located on the dendrites of relay cells and interneurons (Avwenagha et al., 2006). Another intriguing candidate is fibroblast growth factor 15 (Fgf15), a signaling molecule involved in widespread developmental processes including GABAergic differentiation, cell survival, and synapse formation (Hagemann and Scholpp, 2012; Martinez-Ferre et al., 2016). At perinatal ages Ffg15 is expressed along the presumed the migratory path of interneurons, including ventricular layer of the 3rd ventricle, vLGN and dLGN (Gimeno et al., 2003). More importantly, developing RGCs express Ffg15 at perinatal ages during the time when retinal axons innervate dLGN (Kurose et al., 2004). Overall these studies provide an in-depth analysis of dLGN interneuron development and underscore the importance of retinal signaling in the developmental remodeling of their arbors and feedforward inhibitory synapse formation.

SUMMARY AND CONCLUSIONS

These studies addressed the outstanding questions pertaining to the development, form, and function of thalamic interneurons. Here we primarily focused on dLGN, and the manner by which interneurons arrive, distribute, and remodel throughout postnatal development. While the mouse model has provided extraordinary information about the establishment of inhibitory circuits, the migratory path by which dLGN interneurons travel, as well as their morphological development has remained unclear. Furthermore, while it is understood that retinal signaling contributes to some aspects of interneuron dispersion (Golding et al., 2014), we addressed whether retinal axon innervation regulates their targeting, morphology, and synaptic connectivity. To accomplish this, we used the GAD67-GFP transgenic mouse line that labels thalamic interneurons with GFP to track their migration, and conduct in-vitro patch-clamp recordings with biocytin-filled pipettes throughout postnatal life to examine their structure and function. In order to determine how retinal signaling influences these developmental events, we used a genetic deafferentation model and utilized the math5 null mouse (math5$^{-/-}$) to compare with age-matched controls.

In Chapter I, we examined the migratory path by which interneurons follow to arrive in dLGN and addressed the debate about the source of these neurons (Golding et al., 2014; Jager et al., 2016). BDA injections near V3 and into SC confirm that interneurons travel from the neuroepithelium of V3, across the ventral border of VB, and into vLGN. At early ages, interneurons gradually migrate dorsally into dLGN and finish evenly dispersing themselves throughout the nucleus by P4. Similarly, LPN migration and distribution also reaches stable levels by this time. However, in the absence of retinal innervation, fewer interneurons arrive in visual thalamus (vLGN, dLGN, LPN) and neurons remain clustered in the top sectors of nuclei. By contrast, the somatosensory VB complex contained substantially more interneurons, which implies that interneurons are misrouted en-route to their final destination. Together, our findings indicate that retino-recipient nuclei rely on retinal signaling for proper recruitment and integration of inhibitory neurons.

To determine the underlying molecular mechanisms for these defects, we used the Fgf15 knockout transgenic mouse (Fgf15$^{-/-}$) to assess how the loss of this growth factor impacts interneuron migration and distribution. This neurotrophic factor was a plausible candidate because it is involved in GABAergic differentiation (Ornitz and Itoh, 2015; Martinez-Ferre et al., 2016) and is downregulated in math5$^{-/-}$ mice (Fox lab, unpublished observations). Our studies showed that Fgf15$^{-/-}$ regulates interneuron migration to dLGN, but not dispersion within the nucleus. In Fgf15$^{-/-}$ mice, interneurons are misrouted, as there were fewer interneurons in vLGN and dLGN, but VB contained far more.

However, the interneurons that arrive at their destination maintained normal distribution patterns. These results signify the likely possibility that multiple signaling pathways are involved in the establishment of inhibitory circuitries in thalamus that are independent of each other, yet all dependent on retinal axons.

In Chapter II, we discussed how the development of dLGN interneurons is a multi-step process that involves migration (see Chapter I), arbor remodeling, and synapse formation. Arbor remodeling consists of an exuberant branching period, whereby interneuron branch number and complex increase. Such growth is transient however, as interneurons then undergo pruning and stabilization to assume their adult-like architectures. Meanwhile, the emergence of feedforward inhibition occurs around this time (~P14) (Bickford et al., 2010), after intrinsic membrane properties have fully matured. Our results in math5 mutants revealed that the absence of retinal signaling causes numerous developmental disruptions. Structurally, interneurons in math5$^{-/-}$ mice did not experience arbor remodeling, but rather maintained simple architectures at all ages. Functionally, their intrinsic membrane properties remained immature, and interneurons made fewer and/or weaker inhibitory synapses onto relay neurons.

Taken together, our studies demonstrate the essential role of retinal innervation in interneuron targeting, migration, distribution, as well as their morphological and synaptic development. These studies provide a foundation for future experiments that can address the issues that remain unknown regarding the development of thalamic interneurons. For example, although our caspase-3 studies showed negative results during postnatal ages, it is necessary to confirm

whether interneurons in math5$^{-/-}$ mice experience increased apoptotic activity during embryonic development. This will clarify if the loss of dLGN interneurons is caused by misrouted neurons and/or cell death in the absence of retinal signaling. Additionally, the underlying mechanism for interneuron distribution through dLGN is unclear. While our studies show that Fgf15 is vital for their arrival, future studies should explore the role of DSCAMs in the spacing of thalamic interneurons because this cell adhesion molecule is needed for appropriate retinal organization (Fuerst et al., 2012) and its role may extend beyond the retina. Finally, it would be worthwhile for future research to examine the link between the reported phenotypes and behavior. An alteration in inhibitory circuitry such as fewer cells in LPN and increased interneurons in VB may disrupt visuomotor and/or escape behaviors, and/or increase sensitivity to somatosensory stimuli, respectively. The mouse has proven to be an invaluable model system to understand the development of visual thalamus, and building on the results outlined here will further illuminate how thalamic interneurons contribute to functional visual circuits.

REFERENCES

Allen AE, Procyk CA, Howarth M, Walmsley L, Brown TM (2016) Visual input to the mouse lateral posterior and posterior thalamic nuclei: photoreceptive origins and retinotopic order. J Physiol 594:1911-1929.

Arcelli P, Frassoni C, Regondi MC, De Biasi S, Spreafico R (1997) GABAergic neurons in mammalian thalamus: a marker of thalamic complexity? Brain Res Bull 42:27-37.

Avwenagha O, Bird MM, Lieberman AR, Yan Q, Campbell G (2006) Patterns of expression of brain-derived neurotrophic factor and tyrosine kinase B mRNAs and distribution and ultrastructural localization of their proteins in the visual pathway of the adult rat. Neuroscience 140:913-928.

Bickford ME, Carden WB, Patel NC (1999) Two types of interneurons in the cat visual thalamus are distinguished by morphology, synaptic connections, and nitric oxide synthase content. J Comp Neurol 413:83-100.

Bickford ME, Zhou N, Krahe TE, Govindaiah G, Guido W (2015) Retinal and Tectal "Driver-Like" Inputs Converge in the Shell of the Mouse Dorsal Lateral Geniculate Nucleus. J Neurosci 35:10523-10534.

Bickford ME, Slusarczyk A, Dilger EK, Krahe TE, Kucuk C, Guido W (2010) Synaptic development of the mouse dorsal lateral geniculate nucleus. J Comp Neurol 518:622-635.

Blank M, Fuerst PG, Stevens B, Nouri N, Kirkby L, Warrier D, Barres BA, Feller MB, Huberman AD, Burgess RW, Garner CC (2011) The Down syndrome critical region regulates retinogeniculate refinement. J Neurosci 31:5764-5776.

Blitz DM, Regehr WG (2005) Timing and specificity of feed-forward inhibition within the LGN. Neuron 45:917-928.

Borello U, Cobos I, Long JE, McWhirter JR, Murre C, Rubenstein JL (2008) FGF15 promotes neurogenesis and opposes FGF8 function during neocortical development. Neural Dev 3:17.

Brauer K, Schober W (1982) Identification of geniculo tectal relay neurons in the rat's ventral lateral geniculate nucleus. Exp Brain Res 45:84-88.

Brown NL, Patel S, Brzezinski J, Glaser T (2001) Math5 is required for retinal ganglion cell and optic nerve formation. Development.

Brown NL, Kanekar S, Vetter ML, Tucker PK, Gemza DL, Glaser T (1998) Math5 encodes a murine basic helix-loop-helix transcription factor expressed during early stages of retinal neurogenesis. Development 125:4821-4833.

Cavdar S, Bay HH, Yildiz SD, Akakin D, Sirvanci S, Onat F (2014) Comparison of numbers of interneurons in three thalamic nuclei of normal and epileptic rats. Neurosci Bull 30:451-460.

Cheadle L, Tzeng CP, Kalish BT, Harmin DA, Rivera S, Ling E, Nagy MA, Hrvatin S, Hu L, Stroud H, Burkly LC, Chen C, Greenberg ME (2018) Visual Experience-Dependent Expression of Fn14 Is Required for Retinogeniculate Refinement. Neuron.

Chen C, Regehr WG (2000) Developmental remodeling of the retinogeniculate synapse. Neuron 28:955-966.

Cox CL, Sherman SM (2000) Control of dendritic outputs of inhibitory interneurons in the lateral geniculate nucleus. Neuron 27:597-610.

Cox CL, Zhou Q, Sherman SM (1998) Glutamate locally activates dendritic outputs of thalamic interneurons. Nature 394:478-482.

Cullen MJ, Kaiserman-Abramof IR (1976) Cytological organization of the dorsal lateral geniculate nuclei in mutant anophthalmic and postnatally enucleated mice. J Neurocytol 5:407-424.

Dhande OS, Stafford BK, Lim JA, Huberman AD (2015) Contributions of Retinal Ganglion Cells to Subcortical Visual Processing and Behaviors. Annu Rev Vis Sci 1:291-328.

El-Danaf RN, Krahe TE, Dilger EK, Bickford ME, Fox MA, Guido W (2015) Developmental remodeling of relay cells in the dorsal lateral geniculate nucleus in the absence of retinal input. Neural Dev 10:19.

Evangelio M, Garcia-Amado M, Clasca F (2018) Thalamocortical Projection Neuron and Interneuron Numbers in the Visual Thalamic Nuclei of the Adult C57BL/6 Mouse. Front Neuroanat 12:27.

Friedlander MJ, Lin CS, Stanford LR, Sherman SM (1981) Morphology of functionally identified neurons in lateral geniculate nucleus of the cat. J Neurophysiol 46:80-129.

Fuerst PG, Koizumi A, Masland RH, Burgess RW (2008) Neurite arborization and mosaic spacing in the mouse retina require DSCAM. Nature 451:470-474.

Fuerst PG, Bruce F, Rounds RP, Erskine L, Burgess RW (2012) Cell autonomy of DSCAM function in retinal development. Dev Biol 361:326-337.

Gabbott PL, Bacon SJ (1994) Two types of interneuron in the dorsal lateral geniculate nucleus of the rat: a combined NADPH diaphorase histochemical and GABA immunocytochemical study. J Comp Neurol 350:281-301.

Gabbott PL, Somogyi J, Stewart MG, Hamori J (1986) A quantitative investigation of the neuronal composition of the rat dorsal lateral geniculate nucleus using GABA-immunocytochemistry. Neuroscience 19:101-111.

Gimeno L, Brulet P, Martinez S (2003) Study of Fgf15 gene expression in developing mouse brain. Gene Expr Patterns 3:473-481.

Golding B, Pouchelon G, Bellone C, Murthy S, Di Nardo A, Govindan S, Ogawa M, Shimogori T, Luscher C, Dayer A, Jabaudon D (2014) Retinal input directs the recruitment of inhibitory interneurons into thalamic visual circuits. Neuron 81:13.

Govindaiah G, Cox CL (2006) Metabotropic glutamate receptors differentially regulate GABAergic inhibition in thalamus. J Neurosci 26:13443-13453.

Grubb MS, Thompson ID (2003) Quantitative characterization of visual response properties in the mouse dorsal lateral geniculate nucleus. J Neurophysiol 90:3594-3607.

Guido W (2018) Development, form, and function of the mouse visual thalamus. J Neurophysiol 120:211-225.

Guillery RW (1966) A study of Golgi preparations from the dorsal lateral geniculate nucleus of the adult cat. J Comp Neurol 128:21-50.

Hagemann AI, Scholpp S (2012) The Tale of the Three Brothers - Shh, Wnt, and Fgf during Development of the Thalamus. Front Neurosci 6:76.

Hamos JE, Van Horn SC, Raczkowski D, Uhlrich DJ, Sherman SM (1985) Synaptic connectivity of a local circuit neurone in lateral geniculate nucleus of the cat. Nature 317:618-621.

Harding AJ, Halliday GM, Kril JJ (1998) Variation in hippocampal neuron number with age and brain volume. Cereb Cortex 8:710-718.

Harrington ME (1997) The ventral lateral geniculate nucleus and the intergeniculate leaflet: interrelated structures in the visual and circadian systems. Neurosci Biobehav Rev 21:705-727.

Harris RM, Hendrickson AE (1987) Local circuit neurons in the rat ventrobasal thalamus--a GABA immunocytochemical study. Neuroscience 21:229-236.

Hirsch JA, Wang X, Sommer FT, Martinez LM (2015) How inhibitory circuits in the thalamus serve vision. Annu Rev Neurosci 38:309-329.

Hong YK, Chen C (2011) Wiring and rewiring of the retinogeniculate synapse. Curr Opin Neurobiol 21:228-237.

Hooks B, Chen C (2006) Distinct roles for spontaneous and visual activity in remodeling of the retinogeniculate synapse. Neuron 52:11.

Huberman AD, Feller MB, Chapman B (2008) Mechanisms underlying development of visual maps and receptive fields. Annu Rev Neurosci 31:479-509.

Jager P, Ye Z, Yu X, Zagoraiou L, Prekop HT, Partanen J, Jessell TM, Wisden W, Brickley SG, Delogu A (2016) Tectal-derived interneurons contribute to phasic and tonic inhibition in the visual thalamus. Nat Commun 7:13579.

Jaubert-Miazza L, Green E, Lo F-SS, Bui K, Mills J, Guido W (2005) Structural and functional composition of the developing retinogeniculate pathway in the mouse. Visual neuroscience 22:661-676.

Kaas JH, Lyon DC (2007) Pulvinar contributions to the dorsal and ventral streams of visual processing in primates. Brain Res Rev 55:285-296.

Krahe TE, El-Danaf RN, Dilger EK, Henderson SC, Guido W (2011) Morphologically distinct classes of relay cells exhibit regional preferences in the dorsal lateral geniculate nucleus of the mouse. J Neurosci 31:17437-17448.

Kurose H, Bito T, Adachi T, Shimizu M, Noji S, Ohuchi H (2004) Expression of Fibroblast growth factor 19 (Fgf19) during chicken embryogenesis and eye development, compared with Fgf15 expression in the mouse. Gene Expr Patterns 4:687-693.

Leist M, Datunashvilli M, Kanyshkova T, Zobeiri M, Aissaoui A, Cerina M, Romanelli MN, Pape HC, Budde T (2016) Two types of interneurons in the mouse lateral geniculate nucleus are characterized by different h-current density. Sci Rep 6:24904.

Lieberman AR (1973) Neurons with presynaptic perikarya and presynaptic dendrites in the rat lateral geniculate nucleus. Brain Res 59:35-59.

Maffei A, Nataraj K, Nelson SB, Turrigiano GG (2006) Potentiation of cortical inhibition by visual deprivation. Nature 443:81-84.

Martin PR (1986) The projection of different retinal ganglion cell classes to the dorsal lateral geniculate nucleus in the hooded rat. Exp Brain Res 62:77-88.

Martinez-Ferre A, Lloret-Quesada C, Prakash N, Wurst W, Rubenstein JL, Martinez S (2016) Fgf15 regulates thalamic development by controlling the expression of proneural genes. Brain Struct Funct 221:3095-3109.

McIlwain DR, Berger T, Mak TW (2013) Caspase functions in cell death and disease. Cold Spring Harb Perspect Biol 5:a008656.

Monavarfeshani A, Sabbagh U, Fox MA (2017) Not a one-trick pony: Diverse connectivity and functions of the rodent lateral geniculate complex. Vis Neurosci 34:E012.

Montero VM (1991) A quantitative study of synaptic contacts on interneurons and relay cells of the cat lateral geniculate nucleus. Exp Brain Res 86:257-270.

Munsch T, Yanagawa Y, Obata K, Pape HC (2005) Dopaminergic control of local interneuron activity in the thalamus. Eur J Neurosci 21:290-294.

Ornitz DM, Itoh N (2015) The Fibroblast Growth Factor signaling pathway. Wiley Interdiscip Rev Dev Biol 4:215-266.

Parnavelas JG, Mounty EJ, Bradford R, Lieberman AR (1977) The postnatal development of neurons in the dorsal lateral geniculate nucleus of the rat: a Golgi study. J Comp Neurol 171:481-499.

Pfeiffenberger C, Yamada J, Feldheim DA (2006) Ephrin-As and patterned retinal activity act together in the development of topographic maps in the primary visual system. J Neurosci 26:12873-12884.

Roth MM, Dahmen JC, Muir DR, Imhof F, Martini FJ, Hofer SB (2016) Thalamic nuclei convey diverse contextual information to layer 1 of visual cortex. Nat Neurosci 19:299-307.

Seabrook TA, Krahe TE, Govindaiah G, Guido W (2013) Interneurons in the mouse visual thalamus maintain a high degree of retinal convergence throughout postnatal development. Neural Dev 8:24.

Seabrook TA, Burbridge TJ, Crair MC, Huberman AD (2017) Architecture, Function, and Assembly of the Mouse Visual System. Annu Rev Neurosci 40:499-538.

Sherman SM (2004) Interneurons and triadic circuitry of the thalamus. Trends Neurosci 27:670-675.

Simic G, Kostovic I, Winblad B, Bogdanovic N (1997) Volume and number of neurons of the human hippocampal formation in normal aging and Alzheimer's disease. J Comp Neurol 379:482-494.

Spreafico R, Frassoni C, Arcelli P, De Biasi S (1994) GABAergic interneurons in the somatosensory thalamus of the guinea-pig: a light and ultrastructural immunocytochemical investigation. Neuroscience 59:961-973.

Stanford LR, Friedlander MJ, Sherman SM (1981) Morphology of physiologically identified W-cells in the C laminae of the cat's lateral geniculate nucleus. J Neurosci 1:578-584.

Sur M, Sherman SM (1982) Linear and nonlinear W-cells in C-laminae of the cat's lateral geniculate nucleus. J Neurophysiol 47:869-884.

Szentagothai J (1963) The Structure of the Synapse in the Lateral Geniculate Body. Acta Anat (Basel) 55:166-185.

Tamamaki N, Yanagawa Y, Tomioka R, Miyazaki J, Obata K, Kaneko T (2003) Green fluorescent protein expression and colocalization with calretinin, parvalbumin, and somatostatin in the GAD67-GFP knock-in mouse. J Comp Neurol 467:60-79.

Tschetter WW, Govindaiah G, Etherington IM, Guido W, Niell CM (2018) Refinement of Spatial Receptive Fields in the Developing Mouse Lateral Geniculate Nucleus Is Coordinated with Excitatory and Inhibitory Remodeling. J Neurosci 38:4531-4542.

Tucker P, Laemle L, Munson A, Kanekar S, Oliver ER, Brown N, Schlecht H, Vetter M, Glaser T (2001) The eyeless mouse mutation (ey1) removes an alternative start codon from the Rx/rax homeobox gene. Genesis 31:43-53.

Turrigiano GG, Nelson SB (2004) Homeostatic plasticity in the developing nervous system. Nat Rev Neurosci 5:97-107.

Verma AS, Fitzpatrick DR (2007) Anophthalmia and microphthalmia. Orphanet J Rare Dis 2:47.

Vue TY, Aaker J, Taniguchi A, Kazemzadeh C, Skidmore JM, Martin DM, Martin JF, Treier M, Nakagawa Y (2007) Characterization of progenitor domains in the developing mouse thalamus. J Comp Neurol 505:73-91.

Wang SW, Kim BS, Ding K, Wang H, Sun D, Johnson RL, Klein WH, Gan L (2001) Requirement for math5 in the development of retinal ganglion cells. Genes Dev 15:24-29.

Warner CE, Kwan WC, Bourne JA (2012) The early maturation of visual cortical area MT is dependent on input from the retinorecipient medial portion of the inferior pulvinar. J Neurosci 32:17073-17085.

Welker WI (1973) Principles of organization of the ventrobasal complex in mammals. Brain Behav Evol 7:253-336.

Williams SR, Turner JP, Anderson CM, Crunelli V (1996) Electrophysiological and morphological properties of interneurones in the rat dorsal lateral geniculate nucleus in vitro. J Physiol 490 (Pt 1):129-147.

Wilson JR (1986) Synaptic connections of relay and local circuit neurons in the monkey's dorsal lateral geniculate nucleus. Neurosci Lett 66:79-84.

Wilson JR, Hendrickson AE (1981) Neuronal and synaptic structure of the dorsal lateral geniculate nucleus in normal and monocularly deprived Macaca monkeys. J Comp Neurol 197:517-539.

Yamagata M, Sanes JR (2008) Dscam and Sidekick proteins direct lamina-specific synaptic connections in vertebrate retina. Nature 451:465-469.

Zhou NA, Maire PS, Masterson SP, Bickford ME (2017) The mouse pulvinar nucleus: Organization of the tectorecipient zones. Vis Neurosci 34:E011.

CURRICULUM VITA

Naomi Charalambakis

Department of Anatomical Sciences & Neurobiology

511 South Floyd Street, Room 111

Louisville, KY 40202

<u>EDUCATION:</u>

University of Louisville School of Medicine   October 2018

Louisville, KY

M.S./Ph.D, Anatomical Sciences & Neurobiology

GPA: 3.95

University of Kentucky   2010 – 2013

Lexington, KY

B.S.: Pre-Medicine & Psychology

Minor: Mathematics

GPA: 3.80

<u>POLICY/ADVOCACY/LEGISLATIVE EXPERIENCE:</u>

Director and Policy Coordinator, Science Policy   Fall 2016 – Present
And Outreach Group (SPOG)

- Co-founder and current director of the student science engagement organization at the University of Louisville
- Oversee policy and outreach activities throughout the community

- Organize monthly meetings, and maintain communication with state lawmakers, guest speakers, and local science teachers
- Build and manage relationships with outside partners, including other student science policy groups

Research Lab Tour w/ Sen. Rand Paul's   October 2016
Field Representative
- Hosted Field Representative Whitney Meadows for a tour of the labs throughout the department
- Discussed the importance of federal research funding

***Funding Your Future* Advocacy Forum w/ Keynote**   August 2016
Speaker Rep. John Yarmuth (KY-03)
- Prepared a presentation for attendees about how the federal appropriations process operates and provided resources for students/faculty to advocate for increased biomedical research funding
- House Budget Committee Ranking Member Rep. John Yarmuth (KY-03) discussed the appropriations process from his perspective and encouraged attendees to continue advocating for scientific research funding

Society for Neuroscience Capitol Hill Day   March 2016
- Represented SfN as their Early Career Science Policy Ambassador
- Led group meetings with Congressional offices: Sen. Mitch McConnell (KY), Sen. Rand Paul (KY), Sen. Lamar Alexander (TN), Sen. Jeanne Shaheen (NH), Rep. John Yarmuth (KY-03), and Rep. Steny Hoyer (MD-05)

Society for Neuroscience (SfN) Early Career January – December 2016
Science Policy Ambassador

- Served on behalf of SfN as leader for science advocacy in my community
- Organized three local advocacy events and presented on these events at the annual national meeting

Research!America, Science Policy Intern Summer 2015

- Met with members of Congress to discuss science agency appropriations for Fiscal Year 2016
- Provided research and analysis on federal health agency funding trends and other issues salient to science communication/advocacy; presented data to colleagues and board members
- Attended and briefed staff members on congressional committee hearings
- Drafted and disseminated fact sheets focused on the value of research through the prism of specific diseases, including eating disorders, glaucoma, and tuberculosis
- Conducted research for Know Your Candidates Project Election 2016, providing information on each candidate's views regarding health, science, and biomedical research.

Research Lab Tour w/ Rep. John Yarmuth (KY-03) March 2015
Legislative Director

- Hosted Legislative Director Zack Marshall for a tour of the neuroscience labs

Society for Neuroscience Capitol Hill Day   March 2015
- Participated in meetings with members of Congress including: Sen. Mitch McConnell (KY), Sen. Rand Paul (KY), Sen. Lamar Alexander (TN), and Sen. Tom Cotton (AR)

<center>RESEARCH AND CLINICAL EXPERIENCE</center>

University of Louisville School of Medicine   Fall 2013 – Present
Doctoral Candidate, Anatomical Sciences & Neurobiology
Mentor: Dr. William Guido, Ph.D.
- Studied the morphological and synaptic development of dorsal lateral geniculate nucleus (dLGN) interneurons using transgenic mouse lines
- Developed protocol for 3-D neuronal reconstruction with Imaris (Bitplane) software following confocal microscopy
- Performed anatomical/electrophysiological experiments, including pharmacological and whole-cell patch-clamping
- Evaluated data with statistical analysis using SigmaPlot, MiniAnalysis, and Prism GraphPad
- Prepared scientific abstracts, publications, and posters for presentations at professional conferences

University of Kentucky   Fall 2011 – May 2013
Research Assistant, Department of Psychology
Mentor: Dr. Christia Brown, Ph.D.
- Researched the impact of male/female stereotypes on middle-school students
- Performed statistical (SPSS) analysis to examine the influence of peer group interactions on negative behavior/discrimination in schools

University of Kentucky Alcoholism Lab   Summer 2012

Research Assistant, Department of Psychology

- Assisted with data collection for a research study that observed the physical and mental effects of alcohol among adolescents

University of Kentucky Clinic   Summer 2011

Research Assistant, Department of Pediatric Endocrinology

Mentor: Dr. Irene Hong-McAtee, M.D.

- Compiled patients' A1c levels between the years 2008-2011
- Observed and assisted with neonatal thyroid surgeries

COMMUNITY/PROFESSIONAL ACTIVITIES:

Co-organizer, Louisville Science Pathways   Summer 2017

- Created a summer research internship program for students interested in science, but without prior hands-on laboratory experience

Louisville March for Science   April 2017

- Served on the organizing committee to create a sister march to the national March for Science
- Worked to sustain nonpartisan nature of march and keep focus on the value of science
- Recruited speakers, supplies, city permits, and deployed social media to communicate event details

Louisville Regional Science & Engineering Fair   March 2016 – 2017

Advocacy Day

Helped organize Student Advocacy Day at the Capitol in Frankfort, KY for regional science fair winners

- Students met with state policymakers, including the Governor and Lt.
- Governor, and explained their respective science projects

MEMBERSHIPS:

- Society for Neuroscience   2013 – Present
- Career Research Advancement Focused   2016 – Present
  Training Seminar Series Committee
- Kentucky Academy of Sciences (KAS) Science   Fall 2015 – Present
  Education & Advocacy Committee
- Louisville Regional Science & Engineering Fair   Fall 2015 – 2018
  Board Member
- School of Medicine Graduate Student Council,   2016 – 2017
  Graduate Student Representative

HONORS/AWARDS/APPEARANCES:

- Guest Lecturer, Bellarmine University,   April 2018
  IDC 101-26: Science and Society
- Gordon Research Conference Travel Award   February 2018
- Society for Neuroscience Public Advocacy Forum   November 2017
  "*Advocating for Basic Science in a Disease-Focused World*," Panel Member
- University of Louisville "Focused" Video Interview and Article   April 2017
  "*Focused: PhD student wants to 'be that voice in the science community'*"

- Presenter, Girls STEM Collaborative Conference   April 2017
- Kentucky Science Center Award to SPOG   October 2016
  Outstanding Service & Volunteer Work
- 3rd Place Research Poster Winner   April 2016
  SfN Louisville Chapter, Neuroscience Day
- Video Interview, SfN Capitol Hill Day   March 2015
  "Why Advocacy is Important to Me"
- Dean's List, University of Kentucky   Fall 2011 – 2013
- America's Top Chemistry/Physics Students   Fall 2010
- Presidential Scholarship, University of Kentucky   2009 – 2013
- 1st Place Speech Contest, University of Kentucky   March 2011

PUBLICATIONS:

- Abstract, Poster Presentation – *The absence of retinal input affects the targeting, dendritic architecture, and synaptic connectivity of intrinsic interneurons in mouse dLGN,* Gordon Research Conference, February 2018. Lucca, Italy.

- Letter to the Editor, *The New York Times* – "Kentucky and Medicaid," January 21st, 2018

- Letter to the Editor, *The Washington Post* – "The seeds of sexual harassment are planted early" October 20th, 2017.

- Letter to the Editor, *The Lexington Herald Leader* – "House tax bill risks brain drain" November 22nd, 2017

- Featured Interview, *The Washington Post* – "What's changed since the March for Science? Readers respond." By Sarah Kaplan. Oct. 23rd, 2017.

- Letter to the Editor, *The Courier Journal* – "Unity Needed in Health Debate," July 25th, 2017

- Letter to the Editor, *The New York Times* – "Proposed Cuts in the Trump Budget." March 17th, 2017

- Featured Interview, *HuffPost* – "With the Stroke of a Pen, Trump May Have Sparked an American Brain Drain." By Sam Stein. January 20th, 2017.

- Abstract, Poster Presentation – *The absence of retinal input affects the targeting and morphological development of intrinsic interneurons of dLGN*. Society for Neuroscience Conference, Fall 2016. San Diego, CA.

- Abstract, Poster Presentation – *The importance of student advocacy at the science policy intersect: my journey as an early career neuroscientist*. Society for Neuroscience Conference, Fall 2016. San Diego, CA.

- Op-Ed, *The Courier Journal* – "Students Must Advocate for Education", July 18th, 2016.

- Abstract, Poster Presentation – *Developmental Remodeling of intrinsic interneurons in the mouse dorsal lateral geniculate nucleus*. Society for Neuroscience Conference, Fall 2015, Chicago, Illinois.

- Abstract, Poster Presentation – *Optogenetic activation of inhibitory synapses in the dorsal lateral geniculate nucleus of the mouse;* Society for Neuroscience Conference, Fall 2014, Washington, DC

- Video Interview, Society for Neuroscience Capitol Hill Day 2014, "Why Advocacy is Important to Me."

- Medical Student Curriculum, University of Kentucky School of Medicine 2012, "Waisting Time: An Outlook on Eating Disorders."